

Trapped Electron Model 2 (TEM-2)

April 25, 2010

Paul O'Brien and Timothy B. Guild
Space Science Applications Laboratory
Physical Sciences Laboratories

Prepared for:

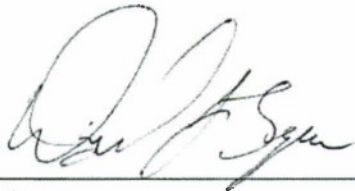
National Reconnaissance Office
14675 Lee Rd.
Chantilly, VA 20151-1715

Authorized by: National Systems Group

APPROVED FOR PUBLIC RELEASE;
DISTRIBUTION UNLIMITED

This report was submitted by The Aerospace Corporation, El Segundo, CA 90245-4691, under Contract No. FA8802-09-C-0001 with the Space and Missile Systems Center, 483 N. Aviation Blvd., El Segundo, CA 90245. It was reviewed and approved for The Aerospace Corporation by J. H. Clemmons, Principal Director, Space Science Applications Laboratory; and G. A. Davis, General Manager, Imagery Programs Division. David Byers was the project officer for the program.

This technical report has been reviewed and is approved for publication. Publication of this report does not constitute NRO approval of the report's findings or conclusions. It is published only for the exchange and stimulation of ideas.

A handwritten signature in cursive script, appearing to read 'David Byers', is positioned above a horizontal line.

David Byers
IMINT R&T

REPORT DOCUMENTATION PAGE			Form Approved OMB No. 0704-0188	
Public reporting burden for this collection of information is estimated to average 1 hour per response, including the time for reviewing instructions, searching existing data sources, gathering and maintaining the data needed, and completing and reviewing this collection of information. Send comments regarding this burden estimate or any other aspect of this collection of information, including suggestions for reducing this burden to Department of Defense, Washington Headquarters Services, Directorate for Information Operations and Reports (0704-0188), 1215 Jefferson Davis Highway, Suite 1204, Arlington, VA 22202-4302. Respondents should be aware that notwithstanding any other provision of law, no person shall be subject to any penalty for failing to comply with a collection of information if it does not display a currently valid OMB control number. PLEASE DO NOT RETURN YOUR FORM TO THE ABOVE ADDRESS.				
1. REPORT DATE (DD-MM-YYYY) 25-04-2010		2. REPORT TYPE		3. DATES COVERED (From - To)
4. TITLE AND SUBTITLE Trapped Electron Model 2 (TEM-2)		5a. CONTRACT NUMBER FA8802-09-C-0001		
		5b. GRANT NUMBER		
		5c. PROGRAM ELEMENT NUMBER		
6. AUTHOR(S) Paul O'Brien and Timothy B. Guild		5d. PROJECT NUMBER		
		5e. TASK NUMBER		
		5f. WORK UNIT NUMBER		
7. PERFORMING ORGANIZATION NAME(S) AND ADDRESS(ES) The Aerospace Corporation Physical Sciences Laboratories El Segundo, CA 90245-4691		8. PERFORMING ORGANIZATION REPORT NUMBER TR-2010(3905)-2		
9. SPONSORING / MONITORING AGENCY NAME(S) AND ADDRESS(ES) National Reconnaissance Office 14675 Lee Rd. Chantilly, VA 20151-1715		10. SPONSOR/MONITOR'S ACRONYM(S) NRO		
		11. SPONSOR/MONITOR'S REPORT NUMBER(S)		
12. DISTRIBUTION/AVAILABILITY STATEMENT Approved for public release; distribution unlimited.				
13. SUPPLEMENTARY NOTES 20120420295				
14. ABSTRACT We present a next-generation radiation specification for the electron radiation belts. The specification includes an empirical model of the statistical variation and spatiotemporal covariation of electron fluxes from 40 keV to 10 MeV in the inner and outer zones, as well as a dynamic full solar-cycle reanalysis, which provides a global snapshot of the electron fluxes every 6 hours from 1992 to 2008. The statistical model is derived from data taken by the S3-3, CRRES, Polar, and SCATHA spacecraft. The reanalysis is driven with data from HEO-1, HEO-3, ICO, and SAMPEX. We validate the reanalysis by comparing a test reanalysis without ICO data to actual ICO observations. The statistical model alone can demonstrate Monte Carlo characterization of uncertainties in radiation specifications for internal charging and total ionizing dose due to electrons. The reanalysis can demonstrate engineering applications, such as a "standard solar cycle" for spacecraft design, as well as scientific applications, such as solar wind correlation studies, initial and boundary conditions for numerical simulations, and principal component analysis. We demonstrate application of the model to radiation specifications and to principal component analysis of the electron belts. Due to the prototype nature of the model, it is insufficiently accurate for definitive conclusions to quantitative investigations.				
15. SUBJECT TERMS Space environment, Radiation belts, Radiation specification models, Radiation belt climatology, Reanalysis				
16. SECURITY CLASSIFICATION OF:			17. LIMITATION OF ABSTRACT	18. NUMBER OF PAGES
a. REPORT UNCLASSIFIED	b. ABSTRACT UNCLASSIFIED	c. THIS PAGE UNCLASSIFIED	Leave blank	19a. NAME OF RESPONSIBLE PERSON Paul O'Brien
				19b. TELEPHONE NUMBER (include area code) 571-307-3978

Acknowledgments

This work was supported under The Aerospace Corporation's Independent Research and Development Program, by NASA LWS Targeted Research and Technology Grant NNG05GM22G, and by the NRO's Proton Spectrometer Belt Research program. A merged Polar/CEPPAD dataset was provided by R. Friedel (LANL). An L-sort version of the SAMPEX PET/ELO data was provided by S. Kanekal (LASP). A revised, temperature-corrected version of the CRRES/HEEF data was provided by G. Ginet (AFRL and MIT/Lincoln Lab). We made extensive use of the IRBEM (formerly ONERA) library of magnetic field models and field line tracing routines. The ICO data was funded by AFRL, and the HEO and SCATHA data were provided by our colleagues at The Aerospace Corporation. The authors thank M. Looper for providing calculated response curves for the HEO and ICO channels. We thank A. Vampola for follow-up discussion regarding his S3-3, CRRES, and other magnetic spectrometers. In addition, the authors would like to thank J. Fennell, J. Roeder, J. B. Blake, J. Mazur, S. Huston, S. Bourdarie, D. Boscher, R. Selesnick, D. Brautigam, C. Roth, R. Quinn, P. Whelan, W. R. Johnston, C. Lindstrom, J. Albert, K. Perry, B. Wie, D. Byers, R. Weigel, D. Kondrashov, Y. Shprits, D. Vassiliadis, J. Koller, and G. Reeves for helpful discussions.

Contents

1	Introduction	1
1.1	Energetic electron hazards to spacecraft	1
1.2	Review of established specification models	1
1.3	Review of other next generation specification models	2
1.4	A different approach: A statistical model	3
2	Statistical prior model	4
2.1	Data used to construct the statistical prior model	8
2.2	Data processing to develop the prior model	9
2.2.1	Binning	9
2.2.2	Daily averaging within bins	11
2.2.3	Computing $\vec{\theta}$ and cov $\delta\vec{\theta}$ in each bin	13
2.2.4	Interpolating to the model grid	13
2.2.5	Flux map diagnostics	15
2.2.6	Computing the errors in the interpolated flux map $\vec{\theta}$	18
2.2.7	Computing spatial and spatiotemporal covariances	19
2.2.8	Principal components	21
2.3	Engineering application: Monte Carlo mission scenarios	22
2.3.1	GEO example	23
2.3.2	GPS example	25
2.3.3	Dose depth curves	28
3	Reanalysis procedures	30
3.1	Stating the data assimilation problem	30
3.2	The likelihood to be maximized	31
3.3	The statistical prior model as a likelihood function	31

3.4	The grid interpolation functions	33
3.5	Measurement functions	34
3.6	Pseudo-Poisson error distribution	34
3.7	Gaussian error distribution	35
4	Reanalysis data	36
4.1	HEO and ICO data	36
4.2	SAMPEX data	38
4.3	Accounting for latent data	38
5	Reanalysis results	43
5.1	Validation and known issues	43
5.2	Engineering application	46
5.3	Science application	46
5.3.1	Empirical determination of the time evolution operator	46
5.3.2	Posterior principal component analysis	47
6	Summary	56
A	TEM-1	57
B	Useful derivatives	58

Figures

1	An example of the Weibull distribution fit to observed fluxes in a selected energy channel in a bin of α_{eq} and L_m . The distribution fits well everywhere except the very lowest 2-3% of the distribution, which is of little consequence for spacecraft effects. The top panel is a quantile-quantile plot, and the bottom panel shows the tails of the cumulative distribution and exceedance probability.	6
2	A pairwise scatter plot of the transformed fluxes, u , for two bins, superimposed on the probability density of the Gaussian copula with correlation parameter 0.71 taken from the data. Contour lines are provided at copula densities of 0 to 4 in steps of 0.5. As expected, the points cluster where the density is high (red).	7
3	Flow chart depicting data processing steps that lead to the prior model data tables.	10
4	TEM-2 data coverage combined over all missions in selected energy ranges.	12
5	Median and 95 th percentile flux maps for one CRRES MEA channel, along with errors on $\tilde{\theta}$ and coverage. A black “X” indicates that an $\alpha_{eq} - L_m$ bin did not meet the bin selection criteria defined in section 2.2.1, usually because of too few days of data.	14
6	TEM-2 maps of median and 95 th percentile fluxes.	16
7	Comparison of TEM-2 to AE8 and CRRESELE along an equatorial radial profile.	17
8	Comparison of TEM-2 to AE8 and CRRESELE along a field line through (4.5,0,0) R_E in the outer zone.	17
9	Comparison of TEM-2 to AE8 and CRRESELE along a LEO trajectory through the South Atlantic Anomaly.	18
10	Median (top) and 95 th percentile (bottom) fluxes. Data from in situ observations in the bin are plotted in color. The nearest neighbors fit is indicated in black. Also shown is the “base θ ” given by 22. Error bars on the points and the fit indicate one standard deviation.	20
11	Comparison of TEM-2 scenarios and reanalysis to AE8 and GOES-10 observations for a real interval. GOES-10 flux is multiplied by 3π to approximate conversion from unidirectional to omnidirectional flux, assuming that the flux follows a $\sin^{5/4} \alpha$ distribution in local pitch angle. CRRESELE, as plotted, is driven by “Ap15”, the 15-day trailing average of the Ap index [Brautigam and Bell, 1995]. The percentiles shown are taken from 200 Monte Carlo scenarios, of which only 20 are shown (gray).	23
12	Comparison of TEM-2 scenarios and GOES-10 observed statistical distribution of > 2 MeV electron flux. The plot format follows that of Figure 1. GOES-10 flux is multiplied by 3π as in Figure 11. The TEM-2 distribution shown is taken from 200 Monte Carlo scenarios.	24
13	10-year environments at GEO. Top: Mean flux from various models; AE8 (MIN and MAX are the same at GEO). Bottom: worst-case 24-hour exponentially-weighted flux average.	26

14	10-year environments at GPS. Top: Mean flux from various models; AE8. Bottom: worst-case 24-hour exponentially-weighted flux average.	27
15	10-year total dose environments at GEO (top) and GPS (bottom).	29
16	Calculated energy response curves for HEO and ICO channels.	37
17	(Top) SAMPEX PET/ELO intensity can be used as a proxy for HEO-3 E5. (Bottom) The parameters of the proxy relationship vary with L shell.	39
18	Autocorrelation for HEO-3 electron fluxes at 1 day lag for all orbit status and energy channels.	41
19	Autocorrelation for HEO-3 electron fluxes at 2 days lag versus the square of the correlation at 1 day lag for all orbit status and energy channels. The good agreement suggests that the HEO-3 autocorrelation is a first-order autoregressive process.	42
20	Flux versus L_m profiles versus time in the TEM-2 Reanalysis: (top) the entire reanalysis, (middle) one year, centered on the July 2004 storm, and (bottom) one month centered on July 24, 2004.	44
21	Validation of TEM-2 reanalysis versus ICO (in and out of sample).	45
22	The first posterior principal component of the TEM-2 reanalysis, for equatorially mirroring electrons.	48
23	The second posterior principal component of the TEM-2 reanalysis. Top: equatorially mirroring electrons. Bottom: selected isocontours.	50
24	The third and fourth posterior principal components of the TEM-2 reanalysis, for equatorially mirroring electrons.	51
25	Top: TEM-2 reanalysis posterior principal components during the October 1998 GEM storm. Lower panels: observed electron flux at GEO, observed solar wind speed, and the magnetic storm-time disturbance index Dst	52
26	TEM-2 reanalysis posterior principal components and measurements during the October 2000 GEM storm, in the format of Figure 25.	53
27	Prediction efficiency of TEM-2 reanalysis posterior principal components with respect to GOES > 2 MeV electron flux, Dst , and solar wind speed (V_{sw}).	54
28	Impulse response of TEM-2 reanalysis posterior principal components with solar wind speed.	55

Tables

1	Data used to build the statistical prior model	9
2	Coefficients of $\tilde{\theta}^{(0)}$	14
3	Data channels used to drive the reanalysis	36
4	Coefficients for 1-day autocorrelation function vs L for HEO-3 fluxes	40
5	ICO out-of-sample validation statistics	43

1 Introduction

We have developed a prototype next generation radiation specification for electrons with energies from 40 keV to 10 MeV trapped in the Earth's magnetic field. We denote this model Trapped Electron Model 2 (TEM-2). Like its immediate predecessor, TEM-1 (unpublished, see Appendix A), TEM-2 was built as a prototype for future design specifications models. However, in addition to its value as a prototype, TEM-2 also facilitates some new kinds of scientific research in the electron belts. We will demonstrate both engineering and scientific applications of TEM-2. TEM-2 is an alpha version of the upcoming AE9 model. Although it demonstrates new scientific and technical capabilities, it incorporates some known but unresolved issues with the underlying data (see section 2.1); therefore quantitative outputs of TEM-2 are too preliminary to be used for satellite design or quantitative science.

We will begin with a review of the importance of energetic electrons for spacecraft design and operations, and then we will review the existing suite of specification models, including other next generation models which are in development. Next, we will describe our own model and its development in detail. We will also demonstrate the model in an engineering application and in a scientific one.

1.1 Energetic electron hazards to spacecraft

Energetic electrons trapped in the Earth's radiation belt typically pose two hazards to spacecraft: total ionizing dose and internal charging. The total ionizing dose hazard arises from the degradation of electronics and materials from accumulated absorption of ionizing radiation. Spacecraft designers must consider ionizing dose from keV to MeV electrons when choosing parts and shielding to reduce the likelihood of premature failure of a spacecraft or subsystem [e.g., *Tribble et al.*, 1999]. Internal charging by energetic electrons is one potential cause of electrostatic discharge (ESD). Energetic electrons can penetrate spacecraft shielding and deposit their charge internal to the spacecraft surface. If a large electrostatic potential builds up before the charge can dissipate, an ESD may occur, leading to phantom commands, short circuits, and a host of other kinds of anomalies [e.g., *NASA-HDBK-4002*, 1999]. Therefore, a spacecraft designer needs a specification of the mean electron environment which leads to total dose specifications, and the worst case environment, which leads to internal charging specifications. Because the mission mean and worst case environments carry uncertainty due to radiation belt dynamics and measurement errors, there is need for next generation radiation specification models that can describe the dynamic variability of the environment and characterize errors in the models themselves [e.g., *Vette*, 1978; *Gussenhoven et al.*, 1994; *Daly et al.*, 1996].

1.2 Review of established specification models

The industry standard for electron radiation specification is the NASA AE8 model [*Vette*, 1991]. This model provides global coverage of the inner and outer belt electrons (McIlwain L_m from 1.2-11) with energies from 0.04 to 7 MeV. Rudimentary dynamic variation in the environment is provided in the form of different specifications for solar maximum and solar minimum.

The AFRL CRRESELE model [*Brautigam and Bell*, 1995] describes electrons with energies from 0.5 to 6.6 MeV, L_m 2.5-6.8, and magnetic latitude below 68 degrees. CRRESELE provides some indication of the dynamic environment in the form of both average and worst-case radiation maps, as well as

distinct radiation maps for various bins of the 15-day average of the Ap magnetic index. Presumably because of its limited spatial and energy coverage, CRRESELE has not been widely adopted.

Finally, *Vampola* [1996] produced an update to AE8-MIN outer zone flux map using data from the MEA instrument on CRRES. Vampola developed a neural network that specified the outer zone electron fluxes based on the preceding few daily averages of the Kp index. He then ran this neural network model over the entire multi-decade history of Kp. He selected solar minimum years from the results and computed an average outer zone.

There is an extensive literature identifying various shortcomings of these models [e.g., *Vette*, 1978; *Gussenhoven et al.*, 1994; *Daly et al.*, 1996]. In this paper, we are concerned mainly with the lack of a model with sufficient energy and spatial coverage that can also provide estimates of the dynamic variability of the environment and errors in the model itself. We note that at the time AE8 and the CRRES models were built, there were few to no data sets of sufficient temporal and energy/spatial coverage to properly describe the global electron dynamics.

1.3 Review of other next generation specification models

The development of a Monte Carlo scenario capability for a radiation belt model is presently unique to our efforts. However, the reanalysis aspect of our effort is similar to several others.

We are aware of other efforts to develop reanalysis models of the electron radiation belts. One effort, at ONERA (Office National d'Etudes et Recherches Aéronautiques) builds on the well-known Salammbô model [*Maget et al.*, 2007]. By adding data assimilation of measurements from LANL sensors on GPS and geosynchronous (GEO) satellites, the ONERA group has obtained promising results, including a first physics-based data assimilation of solar-cycle duration (a “reanalysis”). At present, the data assimilation scheme being used is direct insertion, which seems to work well on multi-day timescales because diffusive transport quickly smooths out the sharp features produced by direct insertion. This effort has produced a model outer zone average on a year-by-year basis for a full solar cycle [*Bourdarie et al.*, 2009].

A second group, the LANL “DREAM” team, is pursuing a more ambitious model that couples the radiation belt into a global model that includes the ring current, plasmasphere and convection electric fields [*Koller et al.*, 2007]. At time of writing, DREAM has produced promising initial results from an uncoupled outer zone model that employs an ensemble Kalman filter for data assimilation of a radial diffusion-only simulation. This model is driven by LANL GEO and GPS data and by data from NASA’s Polar spacecraft.

A third group, the UCLA “VERB” team, is also developing a physics-based data assimilation model. The VERB model has recently been used to compare reanalyses from CRESS and Akebono observations [*Ni et al.*, 2009; *Shprits et al.*, 2007].

We maintain frequent contact with the ONERA, LANL, and UCLA teams, so that our efforts and theirs can complement each other. We collaborate extensively on data intercalibration, since that work would otherwise be duplicated wastefully. We feel that ultimately data assimilation into a physical model (like theirs) will supersede our statistical reanalysis, so that our results can be seen as an early step in the process and as a potential resource for future improvement of their physics-based reanalysis.

1.4 A different approach: A statistical model

Unlike the models described in section (1.3), our model does not include a physics-based numerical simulation. Typically, observations do not fully specify the global state of the radiation belts at any given time. Therefore, the observations are a constraint, but some other information must be used to “fill in” the description of the global state. In physics-based data assimilation, that other information is the “forecast” state provided by integrating the physical equations from some initial condition to the current time. Then, errors in the physical simulation are weighed against observational errors to produce a maximum likelihood estimate of the actual state of the radiation belts—the “analysis”. In regions where there is no data or where the data is of low quality, the forecast prevails; in regions where there is ample, high quality data, the data prevails; elsewhere, the analysis is somewhere in between the data and the forecast. In other words, the forecast is adjusted as little as possible to make it consistent with the observations.

In our statistical reanalysis, the role of the forecast is replaced by the empirical statistical model. This “prior” model describes the likelihood of any given state of the electron belts; thus, we choose the most likely state that is consistent with the data taken in a window around each 6-hour snapshot. The use of a statistical prior rather than physical forecast separates the “filling in” of the energy/spatial domain from specific assumptions about physical processes (energization, loss, transport). Thus, the statistical reanalysis provides a unique opportunity to test physical hypothesis. The statistical model also enables Monte Carlo scenarios that are realistic and portray the variety of possible futures a space mission might encounter. It is the Monte Carlo scenario capability that allows our model to provide error bars and other indications of uncertainty.

2 Statistical prior model

Our model begins with an *a priori* probability model of the statistical variation and energy/spatial covariation of electron fluxes. This “prior” model was developed from historical electron observations. We will describe the mathematical framework for the prior model and the high resolution data that was used to develop it.

The statistical prior model does not include an explicit solar cycle dependence. Under most circumstances, such a dependence is unhelpful, as mission schedules slip, and one would not wish to have to redesign the radiation protection system due to a slip. *NASA-HDBK-4002* [1999, page 22] states “The project manager knowing the mission schedule may wish to assume some risk in order to save project resources, but it is not recommended because of the environmental variation.”

The statistical prior model includes 4 pieces: a spatial map of the distribution of fluxes, an error covariance matrix for the spatial map, a spatial covariance matrix, and a spatiotemporal covariance matrix. In this context, our “spatial” coordinates are energy E , equatorial pitch angle α_{eq} , and McIlwain’s L_m . Throughout this work, we use the Olson-Pfitzer Quiet (OPQ) magnetic field model [Olson and Pfitzer, 1974] added to the IGRF [IGRF, 2009], as this combination approximates the “typical” state of the magnetic field, even if it ignores the dynamics. A more sophisticated dynamic field model would require solar wind or other inputs that are often unknown in the past and are certainly unknown for future missions.

Our energy grid spans 40 keV to 10 MeV in 12 logarithmically spaced points. Our pitch angle grid has 18 points spanning from 5 to 90 degrees in 5 degree steps. Our L_m grid spans from the inner edge at ~ 1.13 to 11 in 27 points, with finer resolution (0.2) in the inner zone gradually increasing to coarser resolution (1.0) in the outer zone. For many computations, we work on a reduced grid which removes points inside the loss cone. This reduced grid has 418 of the possible 486 $\alpha_{eq} - L_m$ points. The total grid size is 5832 points, which reduces to $N_x = 5016$ when the loss cone points are removed.

We have used the loss cone model from AE8 [Vette, 1991] to define the nominal loss cone. Vette provides an empirical formula for the equatorial pitch angle α_{lc} of the atmospheric loss cone:

$$\frac{1}{\sin^2 \alpha_{lc}} = \begin{cases} 0.6572 L_m^{3.452} & L < 2.4 \\ 0.196 L_m^{4.878} & 2.4 \leq L \leq 3.0 \\ 1.4567 L_m^{3.050} & L > 3.0 \end{cases} \quad (1)$$

At $L_m = 1.1293$ the loss cone is 90 degrees at the equator; i.e., there can be no trapped particles below this L_m value. Vette used an IGRF-like magnetic field model to define L_m . By employing the AE8 limits to L_m computed with the Olson-Pfitzer model, we are introducing a slight inconsistency—one we feel confident can be neglected because of the low L_m values at which the atmospheric loss cone is substantial, where Olson-Pfitzer adds little to IGRF. Evolution of the IGRF since AE8 was developed is potentially a bigger issue.

The map of the distribution of fluxes is an extension of the traditional map of the mean flux on a grid. We denote by \vec{x} differential number fluxes of electrons on our model grid. We adapt the flux map concept by including two parameters of the statistical distribution of flux at each energy/spatial grid point. These two parameters are

$$\theta_1 = \log m_{50}, \quad (2)$$

$$\theta_2 = \log(m_{95} - m_{50}), \quad (3)$$

where m_{50} and m_{95} are the 50th and 95th percentiles of the distribution of flux at each grid point. The

inverse is:

$$m_{50} = \exp(\theta_1), \quad (4)$$

$$m_{95} = \exp(\theta_1) + \exp(\theta_2). \quad (5)$$

Throughout this paper, we use log to represent natural logarithm (\log_e). We have chosen the $\vec{\theta}$ parameterization so that $m_{95} > m_{50} > 0$ even when one or both components of $\vec{\theta}$ is negative. We will explain below how we estimate $\vec{\theta}$ at each grid point.

We will need to track the estimation errors in $\vec{\theta}$ to help characterize the impact of measurement uncertainty and the finite-duration of in situ observations on our ability to specify the radiation environment for future missions. We will retain the error in that estimation process in an error covariance matrix $\underline{\underline{S}}^2$, given by:

$$\underline{\underline{S}} = \begin{bmatrix} \underline{\underline{S}}^{(1)} \\ \underline{\underline{S}}^{(2)} \end{bmatrix}, \quad (6)$$

$$\underline{\underline{S}}^2 = \begin{bmatrix} \underline{\underline{S}}^{2(11)} & \underline{\underline{S}}^{2(12)} \\ \underline{\underline{S}}^{2(21)} & \underline{\underline{S}}^{2(22)} \end{bmatrix} = \underline{\underline{S}} \underline{\underline{S}}^T, \quad (7)$$

$$S_{ij}^{2(kl)} = \text{cov}(\delta\theta_k(E_i, \alpha_{eq,i}, L_{m,i}), \delta\theta_l(E_j, \alpha_{eq,j}, L_{m,j})), \quad (8)$$

where $\delta\theta$ is the standard error estimated for θ . We note that in our implementation, $\underline{\underline{S}}$ is not a square matrix, and details of its calculation will be given below in section 2.2.6.

We will need the spatial covariance matrix to ensure that the radiation belts in Monte Carlo scenarios and in the reanalysis are appropriately smooth. The spatial covariance matrix $\underline{\underline{\Sigma}}$ is

$$\Sigma_{ij} = \text{cov}(z_i, z_j), \quad (9)$$

$$z_i = \Phi^{-1}\left(F(x_i; \vec{\theta}^{(i)})\right), \quad (10)$$

where $F(x_i; \vec{\theta}^{(i)})$ is the cumulative marginal distribution for x_i , and Φ is the cumulative distribution of a standard Gaussian (unit normal). The operation $\Phi^{-1}\left(F(x_i; \vec{\theta}^{(i)})\right)$ converts x_i from a variable with the desired marginal distribution to one with a normal distribution. We have shown in [O'Brien, 2005] that the Weibull distribution is an excellent representation of the marginal distribution of electron fluxes at fixed grid points.

Figure 1 compares the observed distribution in a selected bin to the Weibull distribution. In the top panel, a quantile-quantile plot shows that, with the exception of the lowest fluxes in the distribution, the Weibull is a good representation of the distribution. The bottom panel shows a similar result in the form of the cumulative distribution ($P_{<}$, or F) and exceedance probability ($P_{>}$, or $1 - F$).

The transformation from x to z allows us to utilize the wide array of tools for multivariate Gaussians to model the spatial and temporal smoothness of the radiation belts. Formally, we are using a Gaussian copula [see, e.g., Nelsen, 1999], which describes the relationship between x_i and x_j by way of transformed variables (u_i, u_j), where $u_i = F(x_i; \vec{\theta}^{(i)})$, which makes u equivalent to the fraction of the data that falls below x . Both u_i and u_j are uniformly distributed from 0 to 1, but they retain the correlation information for x_i, x_j . By transforming to uniform variables in the $[0, 1]$ domain, we can model the correlation structure independently of the marginal distributions. Figure 2 shows that the scatter plot of transformed daily average flux in two bins clusters in the regions of high probability

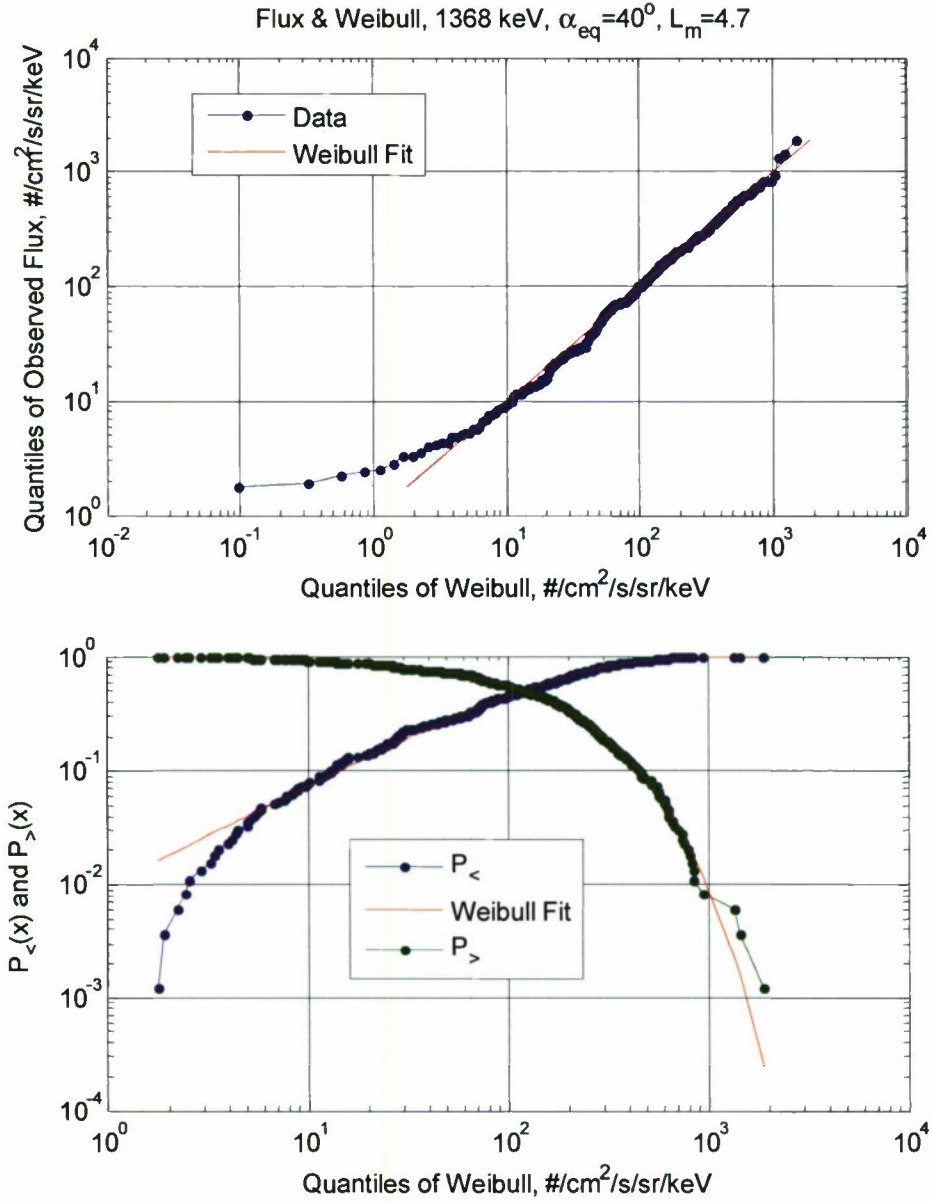


Figure 1: An example of the Weibull distribution fit to observed fluxes in a selected energy channel in a bin of α_{eq} and L_m . The distribution fits well everywhere except the very lowest 2-3% of the distribution, which is of little consequence for spacecraft effects. The top panel is a quantile-quantile plot, and the bottom panel shows the tails of the cumulative distribution and exceedance probability.

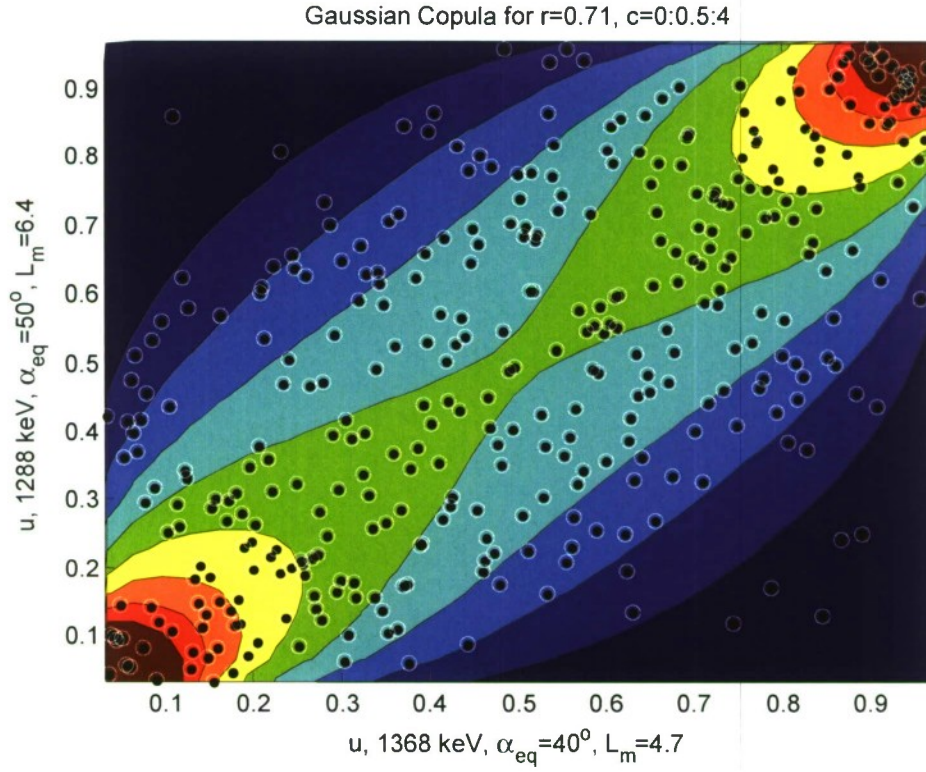


Figure 2: A pairwise scatter plot of the transformed fluxes, u , for two bins, superimposed on the probability density of the Gaussian copula with correlation parameter 0.71 taken from the data. Contour lines are provided at copula densities of 0 to 4 in steps of 0.5. As expected, the points cluster where the density is high (red).

indicated by the copula. The copula has a single parameter for each pair of grid points, which is given by $r_{ij} = \Sigma_{ij}$, our spatial correlation coefficient for the z 's given in (9).

The Weibull distribution is given by:

$$F(x) = 1 - \exp[-(x/x_0)^\gamma], \quad (11)$$

$$\gamma = \frac{\log \left[\frac{\log(1-0.95)}{\log(1-0.50)} \right]}{\log \frac{m_{95}}{m_{50}}}, \quad (12)$$

$$x_0 = \frac{m_{50}}{[-\log(1-0.50)]^{1/\gamma}}. \quad (13)$$

For reference, the average value of a Weibull distribution is given by $x_0 \Gamma(1 + 1/\gamma)$, where $\Gamma(c)$ is the complete Gamma function with argument c .

A useful alternative to the Weibull distribution (one that seems appropriate for the inner zone proton belt), is the log-normal, given by:

$$F(x) = \Phi \left(\frac{\log x - \mu}{\sigma} \right), \quad (14)$$

$$\mu = \log m_{50}, \quad (15)$$

$$\sigma = \frac{\log m_{95} - \mu}{\Phi^{-1}(0.95)}. \quad (16)$$

For reference, the mean of a log normal distribution is given by $\exp(\mu + \sigma^2/2)$

Finally, in order to have appropriate smoothness in time, our model uses a spatiotemporal covariance matrix \underline{R} , which is given by

$$R_{ij} = \text{cov}(z_i(t), z_i(t + \delta t)), \quad (17)$$

where δt is 1 day. \underline{R} gives the correlation at one day lag, which means the model will not effectively describe the variation in the radiation belts on timescales shorter than a day. This is largely a limitation of the observational sampling in L_m and α_{eq} , which are tied to the orbital period of satellites and the spin period of the Earth.

The matrices $\underline{\Sigma}$ and \underline{R} will be processed into \underline{Q} , \underline{G} , and \underline{C} , which are, respectively, the principal components matrix of $\underline{\Sigma}$, the 6-hour persistence operator for the principal components, and the noise conditioning matrix for the principal components. The details of these latter matrices will be given in section 2.3. Together, these data tables, along with $\tilde{\theta}$ and \underline{S} on the model grid, describe, to first order, the statistical properties of the electron belts, along with an indication of the model uncertainty.

2.1 Data used to construct the statistical prior model

To build our statistical prior model, we have used data from CRRES MEA [Vampola *et al.*, 1992], CRRES HEEF [Dichter *et al.*, 1993], S3-3 MES [Vampola and Adams, 1988], SCATHA SC-3 [Reagan *et al.*, 1981], and Polar CEPPAD [Blake *et al.*, 1993]. All of these instruments, to some degree, have calibration errors and backgrounds that ought to be removed. At time of writing, that process is not complete. Instead, we have opted to combine all of the data with nominal calibrations, and assume that the remaining errors and backgrounds will be different enough among the platforms that they will

Table 1: Data used to build the statistical prior model

Vehicle	Interval	Instruments	Energy Coverage	L
S3-3	1976-1979	MES	0.01-1.6 MeV	all
SCATHA	1979-1990	SC-3	0.05-4.6 MeV	5 – 8
CRRES	1991-1992	MEA/HEEF	0.1-7 MeV	2.5-7
Polar	1996-2008	CEPPAD	0.02-10 MeV	all

be smoothed out when we combine the data from multiple sensors. This assumption has largely been proven true. For example, Figure 10 shows a spectral fit of CRRES and SCATHA data in one $\alpha_{eq} - L_m$ bin. At high energies, the SCATHA background causes its spectrum to curve upward, unphysically. However, the nearest-neighbors interpolation and smoothing algorithm smooths out this feature (see section 2.2 for details).

Table 1 provides an overview of the time, energy, and L range of the data used to build the prior model. These data were selected because they are energy- and angle-resolved measurements, so that no sophisticated inversions are required to convert them to the unidirectional differential fluxes need for \vec{x} in the model.

We have filtered out some data which is known to be suspect: CRRES/MEA data for $L_m < 3$, due to possible proton and bremsstrahlung background; the ~ 400 keV channel on Polar/CEPPAD was removed as it is often much higher than neighboring points in the merged IES/HISTe spectrum; S3-3/MES channels 1-4 were removed at the suggestion of Vampola’s data release notes. Known issues that were not addressed include: cosmic ray backgrounds in SCATHA/SC-3, dead-time in Polar/CEPPAD/HISTe, and ion contamination in Polar/CEPPAD/IES. These issues will be addressed in later models (i.e., AE9).

2.2 Data processing to develop the prior model

Figure 3 provides an overview of the data processing steps needed to obtain the model data tables, $\vec{\theta}$, $\underline{\underline{S}}$, $\underline{\underline{G}}$, and $\underline{\underline{C}}$.

The data sets begin as daily files of unidirectional differential flux ($\#/\text{cm}^2/\text{sr}/\text{s}/\text{keV}$) as a function of time. The data are provided either as energy spectra versus time, $x(E_k, \alpha_l, L_{m,t})$, or energy-angle spectra versus time, $x(E_k, \alpha_l, L_{m,t})$. In either case, the pitch angle α is a local pitch angle, and L_m is given for locally mirroring particles only. That is, the angular dependence of L_m is ignored, which introduces a minor inconsistency, but one no worse than the assumption that L_m and α_{eq} are invariant over a particle drift (α_{eq} is a bounce invariant only). Because at this time we have no error estimates for our data, we assume a fixed 10% error for all fluxes: $\delta \log x = 0.1$.

2.2.1 Binning

The first step is to assign the time-series data to $\alpha_{eq} - L_m$ bins so that we can compute statistics over multiple time samples at the same phase-space location. Because we do not know what the best $\alpha_{eq} - L_m$ grid is to begin with, we use a dynamic binning approach to organize each data set. We bin each data set separately. The dynamic binning recursively bisects the α_{eq} and L_m domain to form contiguous bins that meet the following criteria:

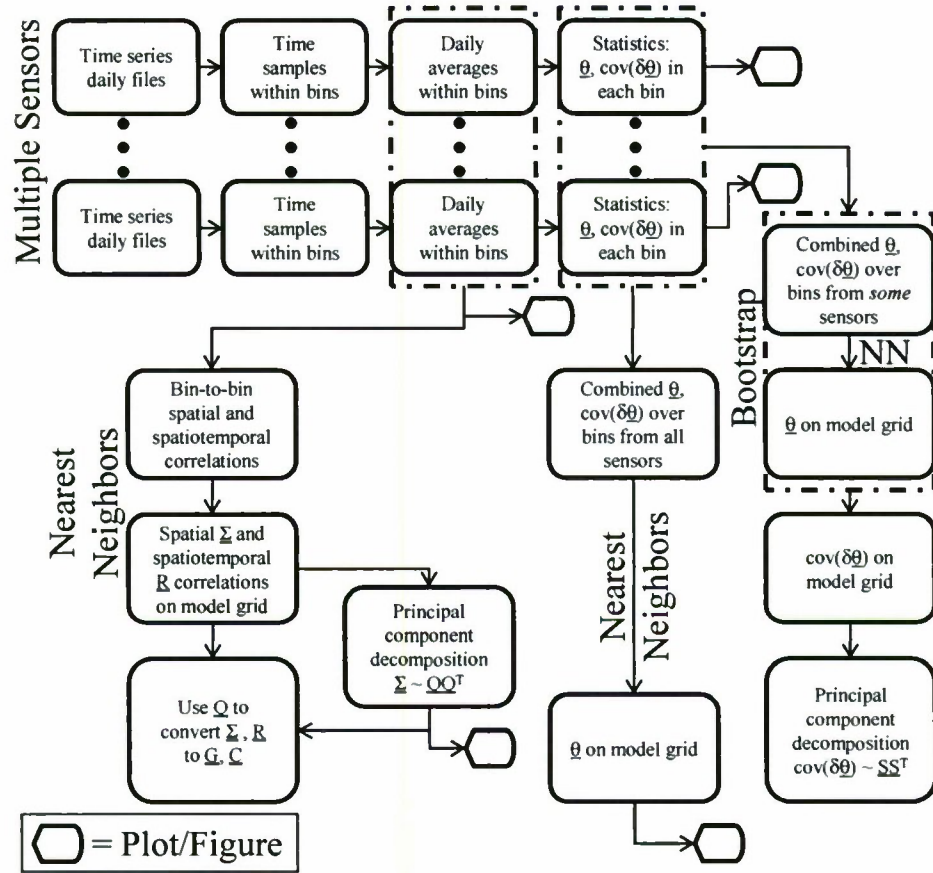


Figure 3: Flow chart depicting data processing steps that lead to the prior model data tables.

- The bin spans at least 1 degree in α_{eq} and 0.05 in L_m ,
- The first and last sample in the bin are separated by at least 182.5 days (1/2 year),
- The bin includes at least 100 unique days of data.

Once the bisection is complete, any bin that spans more than 5 degrees in α_{eq} or 0.25 in L_m is excluded from further processing. This dynamic binning scheme allows us to optimize the $\alpha_{eq} - L_m$ resolution of the flux maps relative to the available data from each mission. We can chose the resolution of the model grid *after* we have already binned the in situ data.

We note that the energy dimension of the bins is slightly different from the α_{eq} and L_m dimensions: each sensor provides fluxes on a unique, but pre-determined, energy grid (the energy channels E_k). Therefore, each sensor on each spacecraft has its own idiosyncratic set of bins in E as well as in α_{eq} , and L_m .

When the binning is complete, each time (and, possibly, angle) sample has been assigned to a $\alpha_{eq} - L_m$ bin. Figure 4 shows the number of days per bin, in selected energy ranges, combined across all the missions in Table 1. CRRES provides a minimum of hundreds of days over nearly the entire domain (see also Figure 5). SCATHA provides a broad band of long-term coverage near GEO at all pitch angles. Polar provides long-term coverage at lower pitch angles.

2.2.2 Daily averaging within bins

Next, we compute daily averages and standard deviations for each bin, in a two-step process. We do this separately for each sensor on each vehicle. First, we compute the average for each pass through the bin during the day, then we compute the average of those passes to give a daily average in the energy/spatial bin. A pass is defined as a set of time samples in the bin with no gaps longer than 15 minutes. In this way, a long pass and a short pass through the same bin would have the same weight in the daily average. This minimizes the impact of serial correlation in the time series data.

The averages are computed with weighting based on the estimated relative error (σ) in the observed fluxes, as follows:

$$\langle x \rangle = \frac{\sum \frac{x_i}{\sigma_i^2}}{\sum \sigma_i^{-2}}, \quad (18)$$

$$\langle x^2 \rangle = \frac{\sum \frac{x_i^2}{\sigma_i^2}}{\sum \sigma_i^{-2}}, \quad (19)$$

$$\sigma_{\langle x \rangle}^2 = \frac{\langle x^2 \rangle}{\langle x \rangle^2} - 1. \quad (20)$$

In the first averaging step (pass-averaging), the weights, σ_i are simply the $\delta \log x$ from the original time series. In the second step (daily-averaging), they are given by the results of (20) in the previous (pass-averaging) step. If, after either step of the averaging process, $\sigma_{\langle x \rangle}$ is less than 0.1, it is replaced by 0.1. Similarly, if it is greater than $\log 10$, it is replaced by $\log 10$. These ad hoc limits ensure that the data analysis process does not idiosyncratically introduce unrealistically small or unrealistically large error bars.

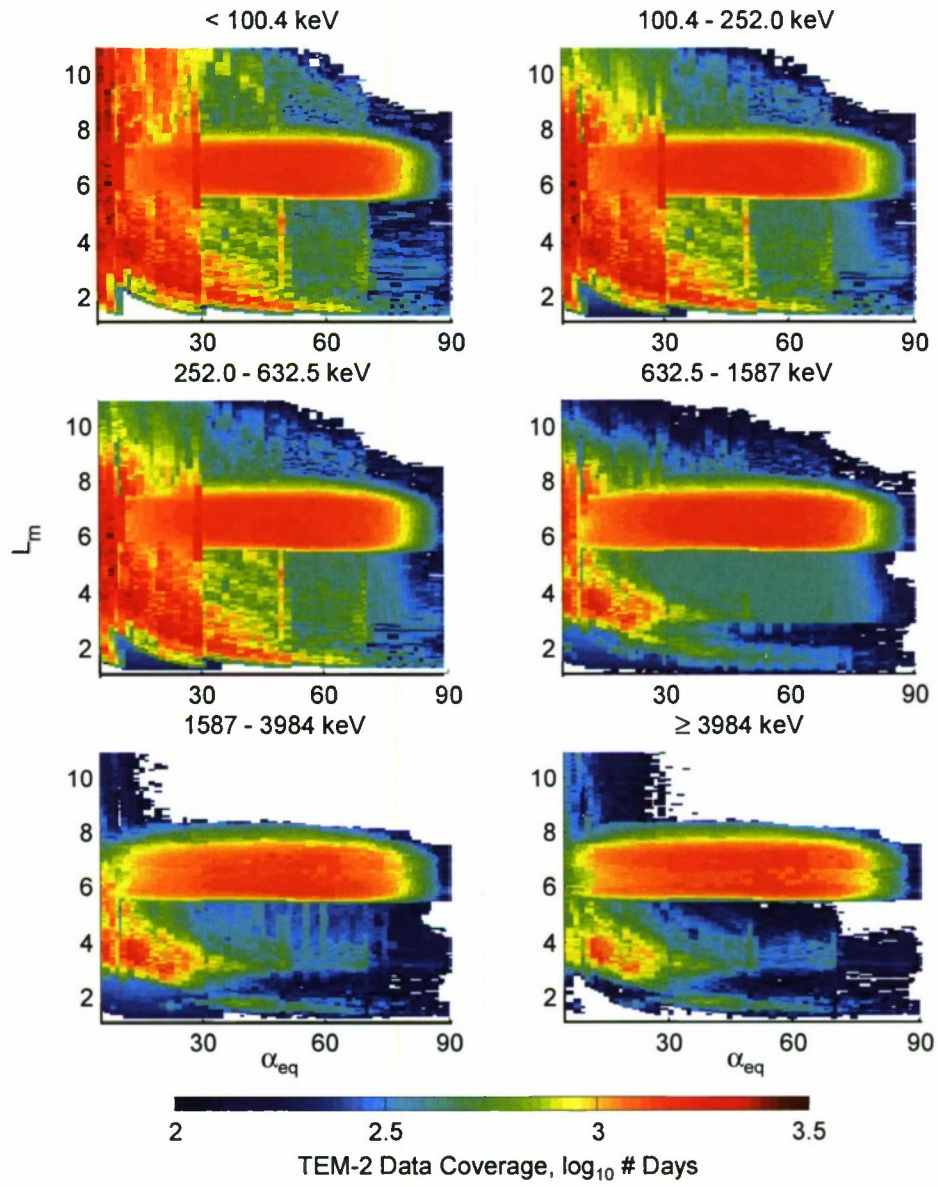


Figure 4: TEM-2 data coverage combined over all missions in selected energy ranges.

2.2.3 Computing $\vec{\theta}$ and $\text{cov } \delta\vec{\theta}$ in each bin

With the data binned and daily averaged, we compute $\vec{\theta}$ for each bin for each sensor on each vehicle. Taking all the data for a particular energy/spatial bin, we perform a bootstrap resampling operation to estimate the error covariance $\text{cov } \delta\vec{\theta}$ in the bin. The bootstrap amounts to randomly resampling the array of daily averages, and then perturbing each selected daily average by a random multiplicative factor $\exp[\sigma_{<x>}\epsilon]$, where ϵ is a random number chosen from a standard normal distribution. This resampling procedure gives us an initial local estimate of $\text{cov } \delta\vec{\theta}$, including the covariance of errors between θ_1 and θ_2 .

We adjust this initial estimate in two ways. First, we inflate the error covariance matrix, if necessary, to account for serial correlation among the daily averages. Let ρ_1 be the linear correlation between adjacent daily averages in the bin. The error covariance should be multiplied by $(1 + \rho_1)/(1 - \rho_1)$ [Zwiers and von Storch, 1995], as a first-order estimate of the effect of serial correlation. Then, this second estimate of the error covariance is rescaled as needed to ensure that the variance of $\delta\theta_1$ and $\delta\theta_2$ are both at least 0.1^2 (i.e., 10% relative error). Conversely, if the variance of either $\delta\theta_k$ is larger than 1 (100% relative error), the associated value of $\vec{\theta}$ is omitted from further analysis because the error is too large. The variance rescaling conserves the linear correlation coefficient implied by the diagonal term in the covariance matrix. We denote the adjusted covariance matrix in bin i with $\underline{s}^{(i)}$:

$$s_{kl}^{(i)} \approx \text{cov}(\delta\theta_k(E_i, \alpha_{eq,i}, L_{m,i}), \delta\theta_l(E_i, \alpha_{eq,i}, L_{m,i})) \quad (21)$$

Figure 5 shows $\vec{\theta}$, errors, error correlation $\left(r(\delta\theta_1, \delta\theta_2) = s_{12}^{(i)} / \sqrt{s_{11}^{(i)} s_{22}^{(i)}}\right)$, and data coverage for one CRRES MEA channel. The lack of data at high L_m arises from the CRRES orbit, and the lack of data at low L_m arises from the removal of $L_m < 3$ data, as indicated in section 2.1. Also, because the orbit was inclined, coverage at high L_m tended to be off the equator, producing a lack of data at high α_{eq} at high L_m . Estimated uncertainty in $\vec{\theta}$ is largest at low L_m , where variability is most dramatic, but the correlation between errors in θ_1 and θ_2 is small.

2.2.4 Interpolating to the model grid

Next, we combine all of the $\vec{\theta}$ from all of the bins from all of the sensors into one global table of $\vec{\theta}(E_i, \alpha_{eq,i}, L_{m,i})$ on the model grid.

First, we fit a “base” model of $\vec{\theta}$ by the method of least squares:

$$\begin{aligned} \theta_i^{(0)}(E, \alpha_{eq}, L_m) &= n_i \log \sin \max[\alpha_{eq} - \alpha_{lc}(L_m), 0.01] \\ &+ a_i - b_i \log E + c_i (L_m - 4.5)^2. \end{aligned} \quad (22)$$

This model amounts to a power law in energy, a roughly \sin^n dependence on equatorial pitch angle, a single belt centered at $L_m = 4.5$, and a loss cone given by (1). The coefficients are given in Table 2.

To interpolate to the model grid, we have taken the average of 120 nearest neighbors. The nearest neighbors are defined in terms of the relative distance from the grid point to the edge of the domain. Equatorial pitch angle and L_m are linearly transformed onto the $[0, 1]$ domain, and energy is transformed logarithmically. Distance in the energy dimension is further scaled down by a factor of 2 to ensure smooth spectra.

CRRES MEA, 876 keV

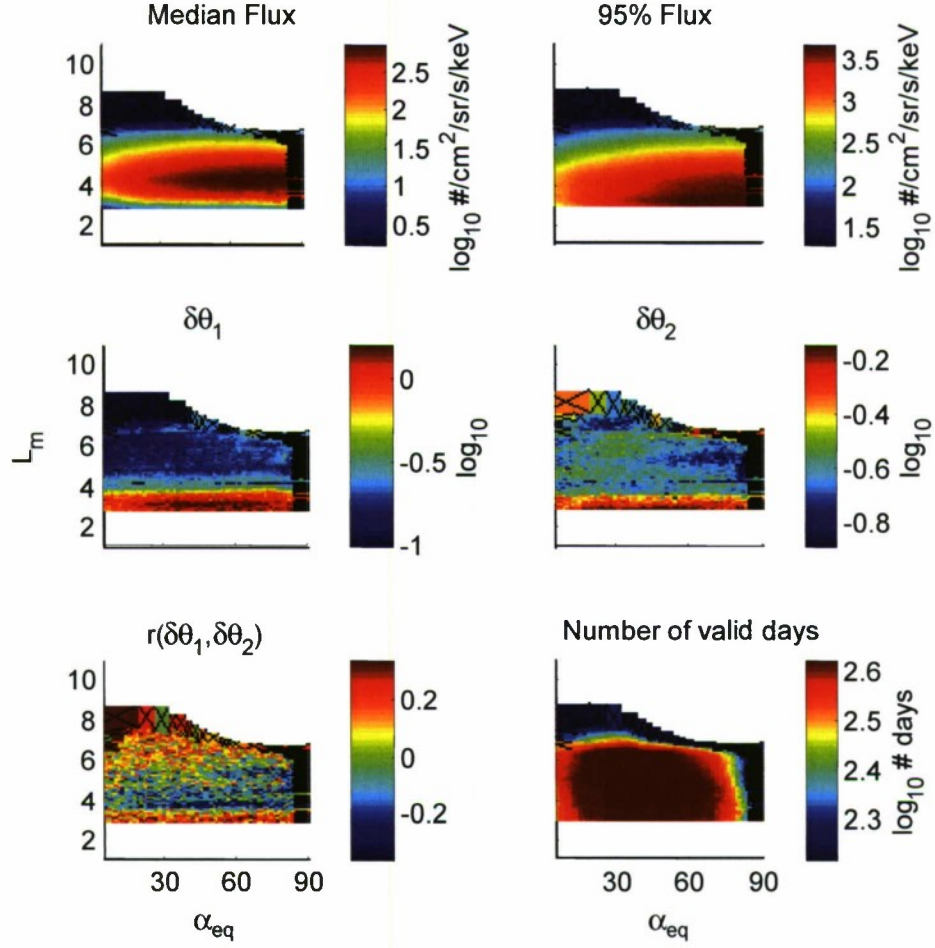


Figure 5: Median and 95th percentile flux maps for one CRRES MEA channel, along with errors on $\vec{\theta}$ and coverage. A black “X” indicates that an $\alpha_{eq} - L_m$ bin did not meet the bin selection criteria defined in section 2.2.1, usually because of too few days of data.

Table 2: Coefficients of $\vec{\theta}^{(0)}$

i	a_i	b_i	n_i	c_i
1	20.6	2.58	0.187	-0.0684
2	21.3	2.41	0.174	-0.0728

We will need the inverse of $\underline{\underline{s}}^{(i)}$ at each grid point, but we will organize this inverse as a large matrix that spans the energy/spatial grid twice on each side rather than as a set of small 2×2 matrices:

$$\zeta_{ij}^{(kl)} = \delta_{ij} \left(\left[\underline{\underline{s}}^{(i)} \right]^{-1} \right)_{kl}, \quad (23)$$

where δ_{ij} is the Kronecker (discrete) delta function.

At each grid point (i), we find the 120 nearest neighbors (j), and compute a weighted average based on weights provided in $\underline{\underline{s}}$ via $\underline{\underline{\zeta}}$.

$$Y_{kj} = \theta_k(E_j, \alpha_{eq,j}, L_{m,j}) - \theta_k^{(0)}(E_j, \alpha_{eq,j}, L_{m,j}), \quad (24)$$

$$\underline{\underline{\Psi}} = \begin{bmatrix} \underline{\underline{\zeta}}^{(11)} \underline{\underline{1}} & \underline{\underline{\zeta}}^{(12)} \underline{\underline{1}} \\ \underline{\underline{\zeta}}^{(21)} \underline{\underline{1}} & \underline{\underline{\zeta}}^{(22)} \underline{\underline{1}} \end{bmatrix}, \quad (25)$$

$$\underline{\underline{\Upsilon}} = \begin{bmatrix} \underline{\underline{\zeta}}^{(11)} \underline{\underline{Y}} + \underline{\underline{\zeta}}^{(12)} \underline{\underline{Y}} \\ \underline{\underline{\zeta}}^{(21)} \underline{\underline{Y}} + \underline{\underline{\zeta}}^{(22)} \underline{\underline{Y}} \end{bmatrix}, \quad (26)$$

$$\begin{bmatrix} \underline{\underline{\vec{\Delta}}}^{(1)} \\ \underline{\underline{\vec{\Delta}}}^{(2)} \end{bmatrix} = \underline{\underline{\Psi}}^{-1} \underline{\underline{\Upsilon}} \quad (27)$$

$$\theta_k(E_i, \alpha_{eq,i}, L_{m,i}) = \Delta_i^{(k)} + \theta_k^{(0)}(E_i, \alpha_{eq,i}, L_{m,i}). \quad (28)$$

After completing this procedure, we have an estimate of $\vec{\theta}$ at each grid point (as opposed to our earlier $\vec{\theta}$ estimates, which were organized in non-uniform bins unique to each sensor). We call this grid of $\vec{\theta}$ a flux map because it can be used to reconstruct the median and 95th percentile fluxes on the model grid.

2.2.5 Flux map diagnostics

In this section, we provide several figures that characterize the flux maps ($\vec{\theta}$). Figure 6 provides $\alpha_{eq} - L_m$ flux maps of the median and 95th percentile fluxes derived from $\vec{\theta}$ according to (4) and (5) at several fiducial energies. The combined flux map is typically not as smooth as the flux maps from individual sensors (e.g., compare to Figure 5). Therefore, in the subsequent development of AE9 and AP9, we expect to revise the nearest-neighbors algorithm.

Figure 7 shows how TEM-2 compares to AE8 and CRRESELE. We have plotted the median from TEM-2 to enable comparison to AE8, which is actually closer to a median flux model than it is to an average flux model [Vette, 1991] (the AE8 flux map results from a least-squares fitting to observed log fluxes, which, for the log-normal distribution used by Vette, results in a fit to the median flux). CRRESELE does not provide a median model, but it does provide an average [Brautigam and Bell, 1995], which allows a rough comparison to AE8 and TEM-2 medians. What we see is that, as expected, the models do not agree quantitatively. Surprisingly, CRRESELE places the outer belt at systematically lower radial distance than does AE8 or TEM-2. That is especially surprising considering that TEM-2 relies heavily on CRRES data. At 1.1 MeV, all of the models are in considerable disagreement as to the location of the major topological features (inner belt, slot, outer belt).

Figure 8 shows the same three models as in Figure 7 but along a field line through the outer zone. Again, disagreement is profound. Generally, it implies that TEM-2 pitch angle distributions are more isotropic (flatter) than those implied in AE8. CRRESELE appears to be the most isotropic (flattest).

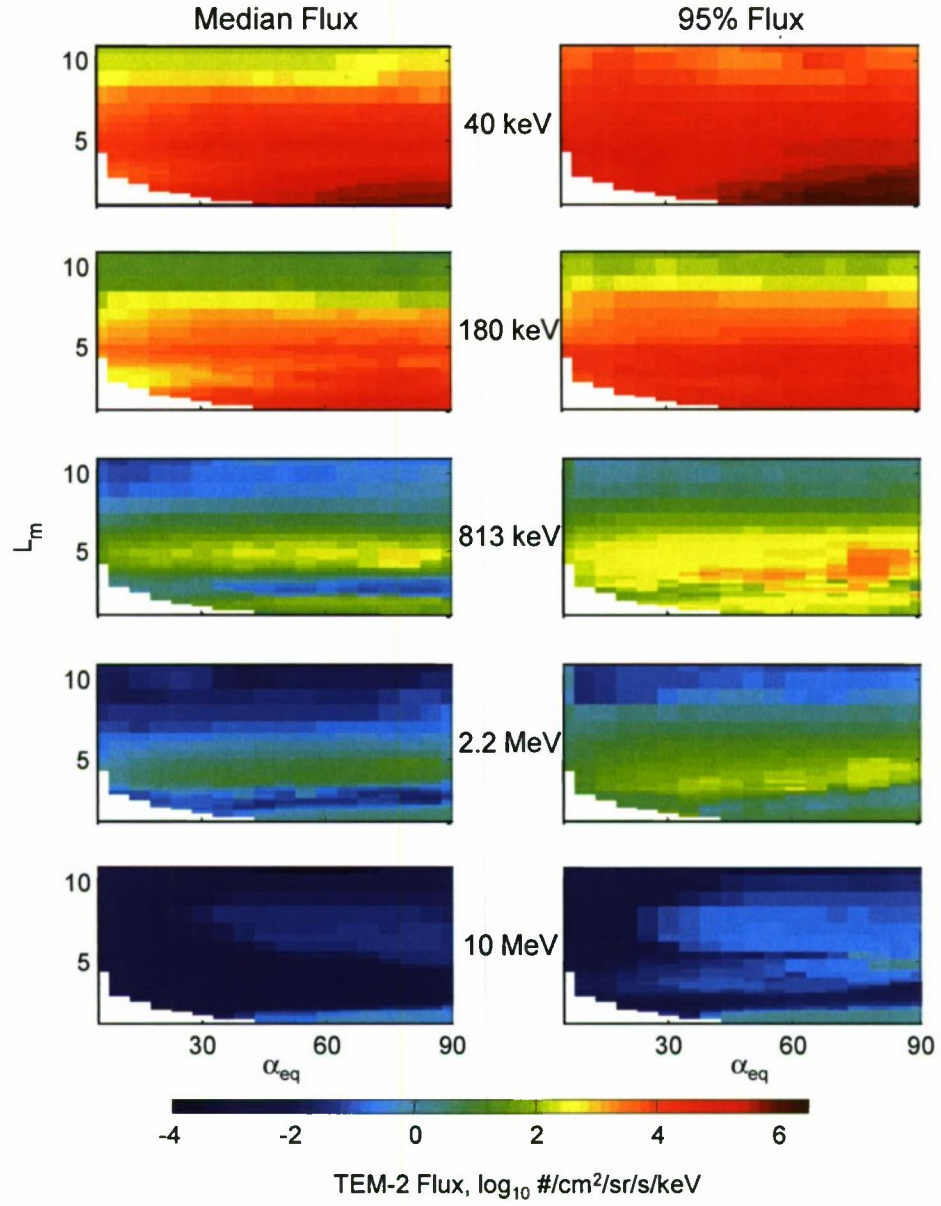


Figure 6: TEM-2 maps of median and 95th percentile fluxes.

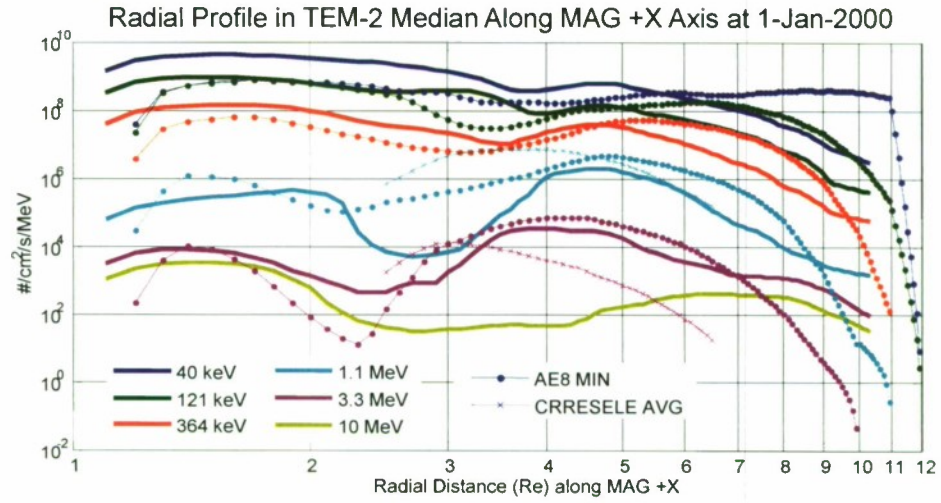


Figure 7: Comparison of TEM-2 to AE8 and CRRESELE along an equatorial radial profile.

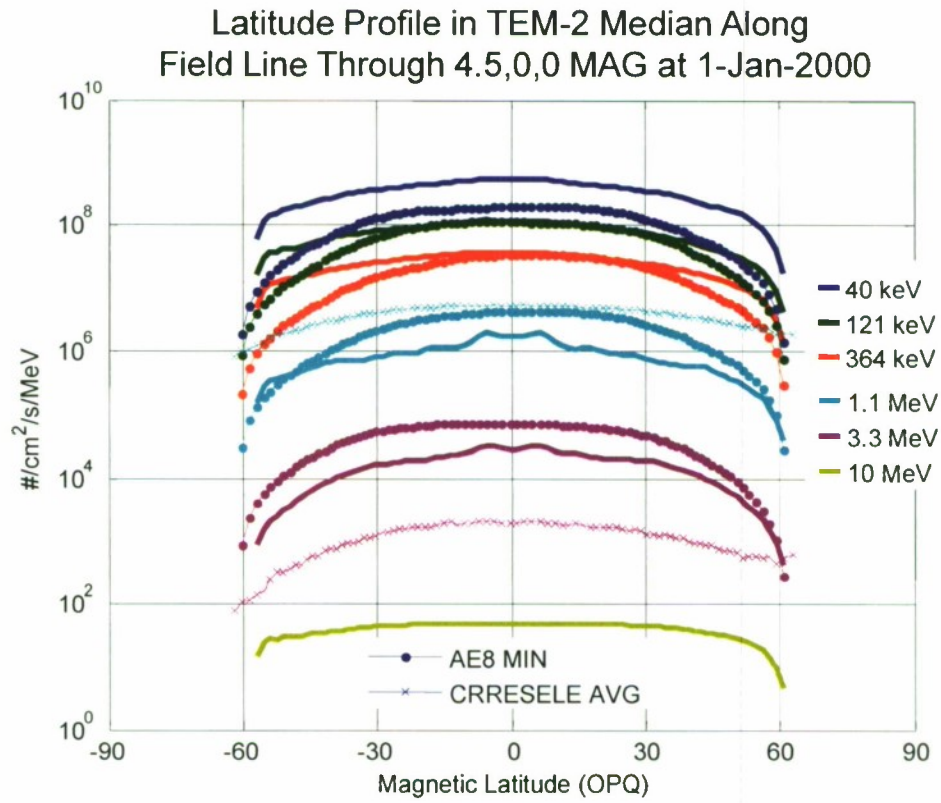


Figure 8: Comparison of TEM-2 to AE8 and CRRESELE along a field line through (4.5,0,0) R_E in the outer zone.

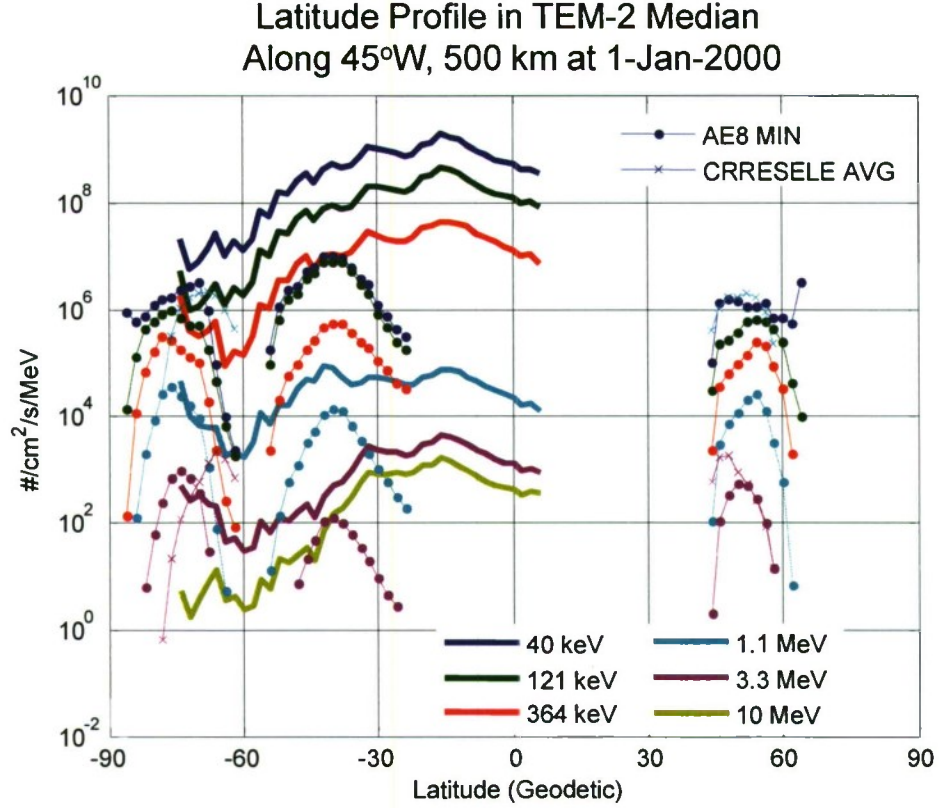


Figure 9: Comparison of TEM-2 to AE8 and CRRESELE along a LEO trajectory through the South Atlantic Anomaly.

Figure 9 shows the same three models as in Figure 7 but along a low altitude longitude line through the South Atlantic Anomaly. Yet again, disagreement is profound. Even though TEM-2 and AE8 parameterized their loss cones the same way in terms of L_m , it appears that the differences between IGRF and OPQ cannot be neglected when defining the maximum ratio of the mirror to equatorial field strength. There is also the possibility that the naive treatment of the angular response of the sensor data has led to an artificially full loss cone. Specifically, a wide-angle sensor can still observe particles in its aperture when looking directly along the field line, giving the incorrect impression of particles in the loss cone.

2.2.6 Computing the errors in the interpolated flux map $\tilde{\theta}$

The error covariance $\underline{\underline{S}}^2$ for the $\tilde{\theta}$ flux map is computed in a bootstrap fashion, where we bootstrap the $\tilde{\theta}$ flux map calculation over random resamples of the set of missions from which the $\tilde{\theta}$ flux map was derived. Our assumption is that each mission may have its own residual systematic errors in the flux map it would produce in isolation. Those errors arise from calibration differences between sensors on different missions and from differences in the natural environment experienced by each mission. By bootstrapping over missions, we include in $\underline{\underline{S}}$ a spatially-correlated measurement error in addition to the local measurement error $\underline{\underline{s}}^{(i)}$ in (21).

In each bootstrap, we also randomly perturb each $\vec{\theta}^{(i)}$, assuming the errors have zero mean with covariance given by $\underline{\underline{S}}^{(i)}$. This perturbation propagates the local error (finite sample size, measurement residual) in $\vec{\theta}^{(i)}$ through the bootstrap, into $\underline{\underline{S}}$.

We compute $\underline{\underline{S}}$ directly from $N_{bs} = 50$ bootstrap solutions for $\vec{\theta}$:

$$S_{i,m}^{(k)} = (\theta_i^{(k,m)} - \bar{\theta}_i^{(k)}) / \sqrt{N_{bs} - 1}, \quad (29)$$

$$\bar{\theta}_i^{(k)} = \frac{1}{N_{bs}} \sum_{m=1}^{N_{bs}} \theta_i^{(k,m)}, \quad (30)$$

where m identifies the m^{th} bootstrap sample. With this definition, $\underline{\underline{S}}\underline{\underline{S}}^T$ is the maximum likelihood estimate of the covariance matrix for $\vec{\theta}$ given the bootstrap samples.

Figure 10 shows the spectrum of median and 95th percentile fluxes in one $\alpha_{eq} - L_m$ bin for three spacecraft and for the nearest-neighbors fit, with error bars. For the most part, as expected, the data lies near the fit. The spread of the data is not large in this bin, and the various measurements all agree fairly well. This is not always the case, but documenting the variety of types of disagreement between the measurements is premature, as the data have not yet been intercalibrated.

2.2.7 Computing spatial and spatiotemporal covariances

The calculation of spatial ($\underline{\underline{\Sigma}}$) and spatiotemporal ($\underline{\underline{R}}$) covariances poses a significant computational problem. We have elected to calculate a limited set of covariances between daily-averaged fluxes in bins from different sensors, and then to interpolate that set of covariances onto the model grid by taking the average of nearest neighbors. We have chosen to compute 3×10^5 spatial covariances and twice that many spatiotemporal covariances. We require at least 100 common days (offset by 1 when computing the spatiotemporal covariance) between any two bins in order to compute a valid covariance.

According to (9) and (17), we must compute the covariances on Gaussianized variables z , which are transformed from the observed fluxes. A member of the set of observed daily average fluxes in a bin is denoted x_i . We denote the position x_i would have in a sorted set from least to greatest as j_i , with positions indexed from 1 to N . We can then empirically convert from x_i to z_i as follows:

$$z_i = \Phi^{-1} \left(\frac{j_i}{N+1} \right) \quad (31)$$

This empirical formula allows us to convert observed fluxes to Gaussian variables without explicitly assuming a marginal distribution (e.g., Weibull). The covariance is then computed between the \vec{z} from one bin and the \vec{z} from another bin.

To interpolate to the model grid, we have taken the average of 10 nearest neighbors, using the same transformed coordinates we used for $\vec{\theta}$, but without the energy dimension scaling factor, and without any error weighting. We note that for covariance calculations the nearest neighbors are in a 6 dimensional space. Although there is considerable error in the computed spatial and spatiotemporal covariances, we neglect it in further calculations because we only need a first-order model of spatial and spatiotemporal covariance.

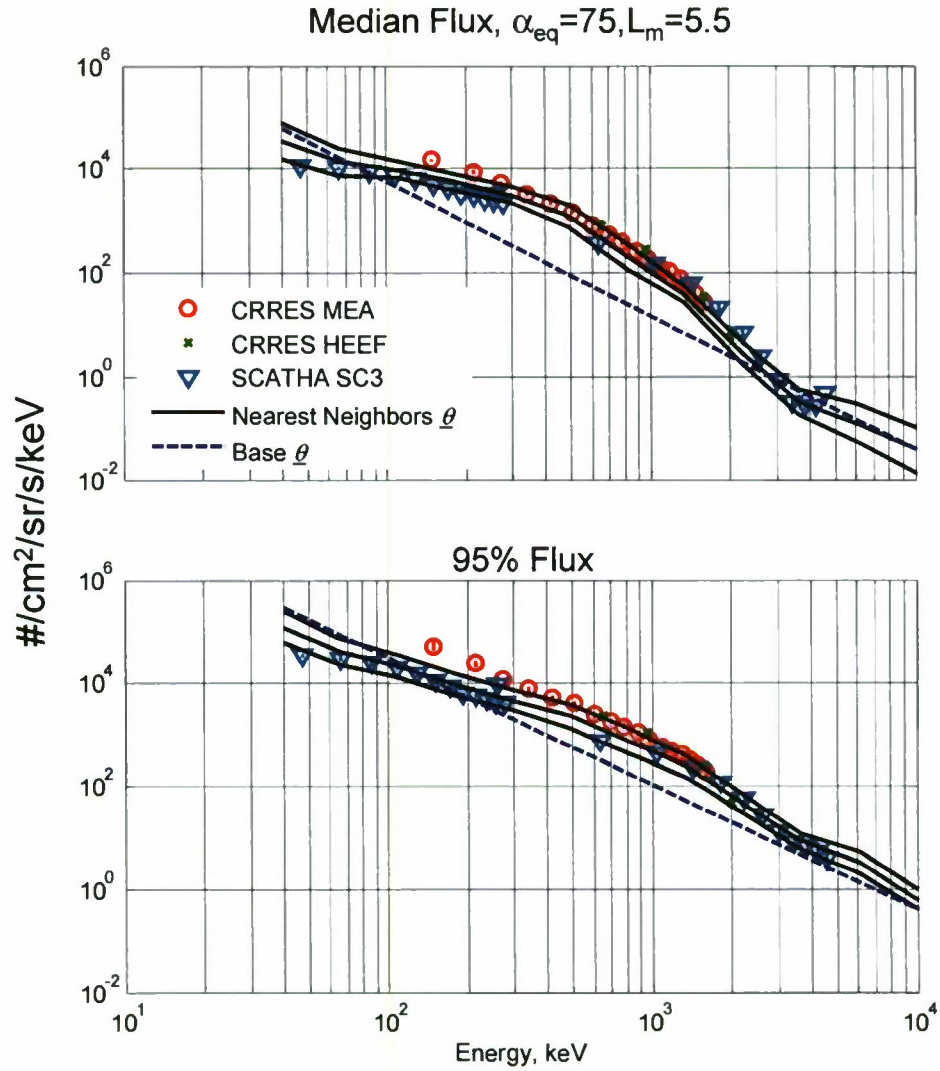


Figure 10: Median (top) and 95th percentile (bottom) fluxes. Data from in situ observations in the bin are plotted in color. The nearest neighbors fit is indicated in black. Also shown is the “base θ ” given by 22. Error bars on the points and the fit indicate one standard deviation.

2.2.8 Principal components

The computed spatial covariance matrix $\underline{\underline{\Sigma}}$ is singular and typically not positive definite, as is common for large covariance matrices, especially those constructed from the kind of sparse spatial coverage we have in the radiation belts. Subsequent operations in the development and use of TEM-2 imply the inverse of $\underline{\underline{\Sigma}}$. To avoid explicitly computing $\underline{\underline{\Sigma}}^{-1}$ we employ a linear change (and reduction) of variables from $\underline{\underline{z}}$ to $\underline{\underline{q}}$ that will represent most of the variation in the $\underline{\underline{z}}$'s while having a non-singular, positive definite covariance matrix.

The transform will have the following form:

$$\underline{\underline{z}} = \underline{\underline{Q}} \underline{\underline{q}}. \quad (32)$$

To construct $\underline{\underline{Q}}$, we first compute the eigen-values and eigen-vectors of $\underline{\underline{\Sigma}}$:

$$\langle \underline{\underline{z}} \underline{\underline{z}}^T \rangle = \underline{\underline{\Sigma}} = \underline{\underline{V}} \underline{\underline{D}} \underline{\underline{V}}^T \approx \underline{\underline{Q}} \underline{\underline{Q}}^T. \quad (33)$$

The columns of $\underline{\underline{V}}$ are orthonormal, and they represent the principal components of variation of the transformed fluxes $\underline{\underline{z}}$. $\underline{\underline{D}}$ is a diagonal eigenvalue matrix with nonincreasing values d_i along the diagonal. *Wilks* [1995, pp. 380-383] reviews a number of methods for selecting how many principal components to retain. All of those heuristics selected principal components of $\underline{\underline{\Sigma}}$ that are clearly noise. Therefore, in a somewhat ad-hoc manner, we select all the principal components that explain more than 1% of the variance over all gridpoints (i.e., $D_{ii} \geq N_x/100$). The other components are, we presume, noise.

Thus we construct $\underline{\underline{\hat{V}}}$ and $\underline{\underline{\hat{D}}}$ by retaining only the first $N_q = 8$ columns of $\underline{\underline{V}}$ and the first N_q rows and columns of $\underline{\underline{D}}$. Our initial estimate of $\underline{\underline{Q}}$ is then

$$\underline{\underline{\hat{Q}}} = \underline{\underline{\hat{V}}} \underline{\underline{\hat{D}}}^{1/2}. \quad (34)$$

However, because we have left out some eigenvalues, we know that $\underline{\underline{\hat{Q}}} \underline{\underline{\hat{Q}}}^T$ only approximates $\underline{\underline{\Sigma}}$. We will need a refined estimate of $\underline{\underline{Q}}$ that preserves unit variance for all the $\underline{\underline{z}}$'s. That is, we need to scale $\underline{\underline{Q}}$ so that the diagonal elements of $\underline{\underline{Q}} \underline{\underline{Q}}^T$ are one.

The correction matrix follows from:

$$\hat{A}_{ij} = \delta_{ij} (\underline{\underline{\hat{Q}}} \underline{\underline{\hat{Q}}}^T)_{ii}. \quad (35)$$

We can now define $\underline{\underline{Q}}$ and its pseudoinverse as $\underline{\underline{Q}}^\dagger$ as:

$$\underline{\underline{Q}} = \underline{\underline{\hat{A}}}^{-1/2} \underline{\underline{\hat{V}}} \underline{\underline{\hat{D}}}^{1/2}, \quad (36)$$

$$\underline{\underline{Q}}^\dagger = \underline{\underline{\hat{D}}}^{-1/2} \underline{\underline{\hat{V}}}^T \underline{\underline{\hat{A}}}^{1/2}. \quad (37)$$

Thus we have avoided the problem that $\underline{\underline{\Sigma}}$ is singular by eliminating the redundant variables. The role of $\underline{\underline{\Sigma}}^{-1}$ is now played implicitly by $\underline{\underline{\Sigma}}^\dagger = (\underline{\underline{Q}}^\dagger)^T \underline{\underline{Q}}^\dagger$.

Because the transform from $\underline{\underline{q}}$ to $\underline{\underline{z}}$ is linear with no additive offset, the $\underline{\underline{q}}$'s are Gaussians with mean zero. Because the $\underline{\underline{q}}$'s are the coefficients of the eigenvectors of $\underline{\underline{\Sigma}}$, the covariance matrix for the $\underline{\underline{q}}$'s is

simply \underline{I} ; that is, the q 's are linearly independent unit Gaussians. The q 's represent the amplitudes of the principal independent, normalized components of the energy/spatial structure of the electron belts. They are loosely analogous to the principal Fourier components of a simple harmonic oscillator after a low-pass filter.

2.3 Engineering application: Monte Carlo mission scenarios

If we can generate a realistic surrogate time series of \vec{q}_t , then we can transform back into fluxes $\vec{q} \rightarrow \vec{z} \rightarrow \vec{x}$ to obtain a realistic surrogate time series of global fluxes. Such a surrogate time series retains the statistical distribution and spatial covariances of the fluxes, and can be used as a Monte Carlo mission scenario for engineering.

In order to generate a realistic series \vec{q}_t , we must use \underline{R} and \underline{Q} to construct a first-order autoregressive (AR1) process for the q 's that will yield the right spatiotemporal covariance of the fluxes, as well. An AR1 process for \vec{q} can be written as:

$$\vec{q}_{t+\delta t} = \underline{G}\vec{q}_t + \underline{C}\vec{\eta}_{t+\delta t}, \quad (38)$$

where $\vec{\eta}_t$ is uncorrelated standard Gaussian white noise, and we initialize \vec{q}_0 to uncorrelated standard Gaussian white noise.

With some matrix manipulations, we can obtain:

$$\underline{G} = \left[\underline{Q}^\dagger \underline{R}^T \left(\underline{Q}^\dagger \right)^T \right]^{\delta t/T}, \quad (39)$$

$$\underline{C} = \left(\underline{I} - \underline{G}\underline{G}^T \right)^{1/2}. \quad (40)$$

The matrix powers are taken via eigenvalue decompositions. During this operation, the eigenvalues of \underline{G} are limited to lifetimes of 3 years, and imaginary eigenvalues of \underline{C} are set to zero. These numerical corrections prevent unrealistically long-lived or growing eigenmodes and imaginary values. As it turns out, in the final build of TEM-2, neither of these corrections was needed.

Using equation (38), we can generate an arbitrary number of realistic scenarios for \vec{q}_t and, in turn, \vec{x}_t . That is, we can generate an arbitrary number of realistic Monte Carlo scenarios for the time series of the global flux environment over the mission. It is then a relatively simple matter to compute from each time-dependent global flux scenario the time series of flux at a notional spacecraft as it moves along its orbit over a mission. For each scenario, we can compute desired engineering quantities, such as total mission dose versus depth, or worst case T-hour fluence.

In order to capture the measurement error, i.e., our uncertainty in the underlying flux map $\vec{\theta}$, we perturb the $\vec{\theta}$ to a unique $\vec{\tilde{\theta}}$ map for each scenario, according to:

$$\begin{aligned} \tilde{\theta}_k(E_i, \alpha_{eq,i}, L_{m,i}) &= \theta_k(E_i, \alpha_{eq,i}, L_{m,i}) \\ &+ \sum_j S_{ij}^{(k)} \epsilon_j, \end{aligned} \quad (41)$$

where each ϵ_j is a random number chosen independently from a standard Gaussian distribution, and \underline{S} is given by (6).

Thus, even in long missions, for which dynamic variability may average out, each scenario will give a slightly different effect (e.g., total dose) consistent with our uncertainty in $\vec{\theta}$.

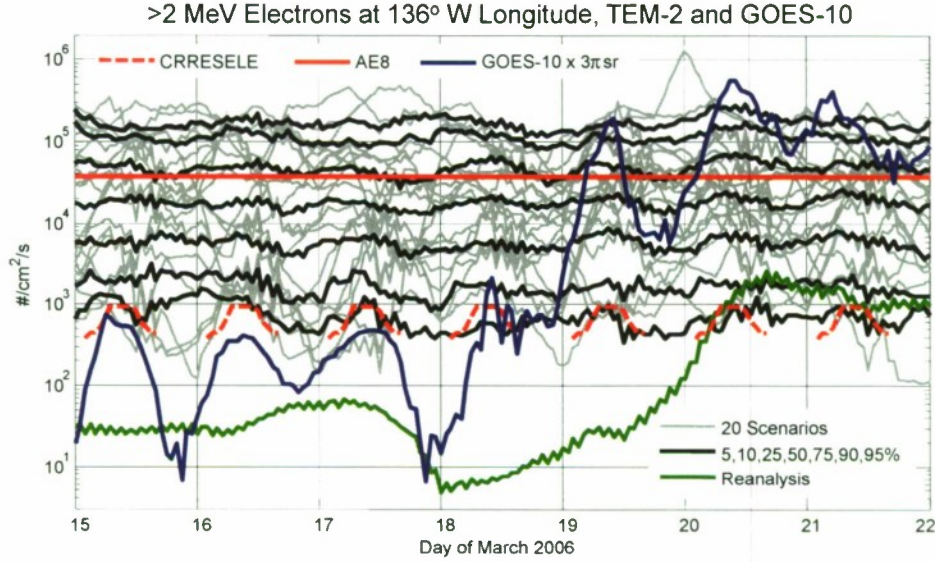


Figure 11: Comparison of TEM-2 scenarios and reanalysis to AE8 and GOES-10 observations for a real interval. GOES-10 flux is multiplied by 3π to approximate conversion from unidirectional to omnidirectional flux, assuming that the flux follows a $\sin^{5/4} \alpha$ distribution in local pitch angle. CRRESELE, as plotted, is driven by “Ap15”, the 15-day trailing average of the Ap index [Brautigam and Bell, 1995]. The percentiles shown are taken from 200 Monte Carlo scenarios, of which only 20 are shown (gray).

2.3.1 GEO example

Figure 11 shows a short interval of a comparison between TEM-2 (including several Monte Carlo scenarios) and observed GOES > 2 MeV electron flux. As expected, quantitative agreement is poor—in fact, GOES-10 spends a significant amount of time measuring fluxes well below the 5th percentile computed from 200 scenarios. However, the different TEM-2 scenarios show some of the diurnal variation evident in the GOES data, and they clearly show dynamic behavior, which is absent from AE8. The very short timescale jagged oscillations on the timescale of an hour or so are likely numerical artifacts of the calculation of the magnetic coordinates.

What the TEM-2 prior model is really built to do is represent the long-term distribution of electron flux along any orbit. Figure 12 shows a comparison of statistical distributions from TEM-2 scenarios versus GOES-10 for > 2 MeV electron flux. The format is the same as Figure 1. The top panel shows that the distribution produced by TEM-2 can be off by as much as a factor of 10 from that of GOES-10, and it does not, generally have the same shape. The only part of the distribution that TEM-2 represents well is the highest 5%. Preliminary results with the AE9 beta reveal that the shape problem will be resolved, but there will be some residual offset (factor of ~ 3). Therefore, we can attribute the shape discrepancy to our choice of magnetic coordinates and the absence of GEO data in TEM-2.

Extending the simulation shown in Figure 11 to an entire 10-year interval, Figure 13 provides spectra of means and 24-hour (exponentially-weighted) worst cases for various models, including TEM-2. These worst-case spectra are an approximation to what one would need for assessing an internal charging hazard. In practice it would be better to run an actual time-dependent internal charging calculation for each scenario and compute statistics from its results. Nonetheless, for comparison to other models, it is necessary to present the worst case computed as a running average flux. Included in

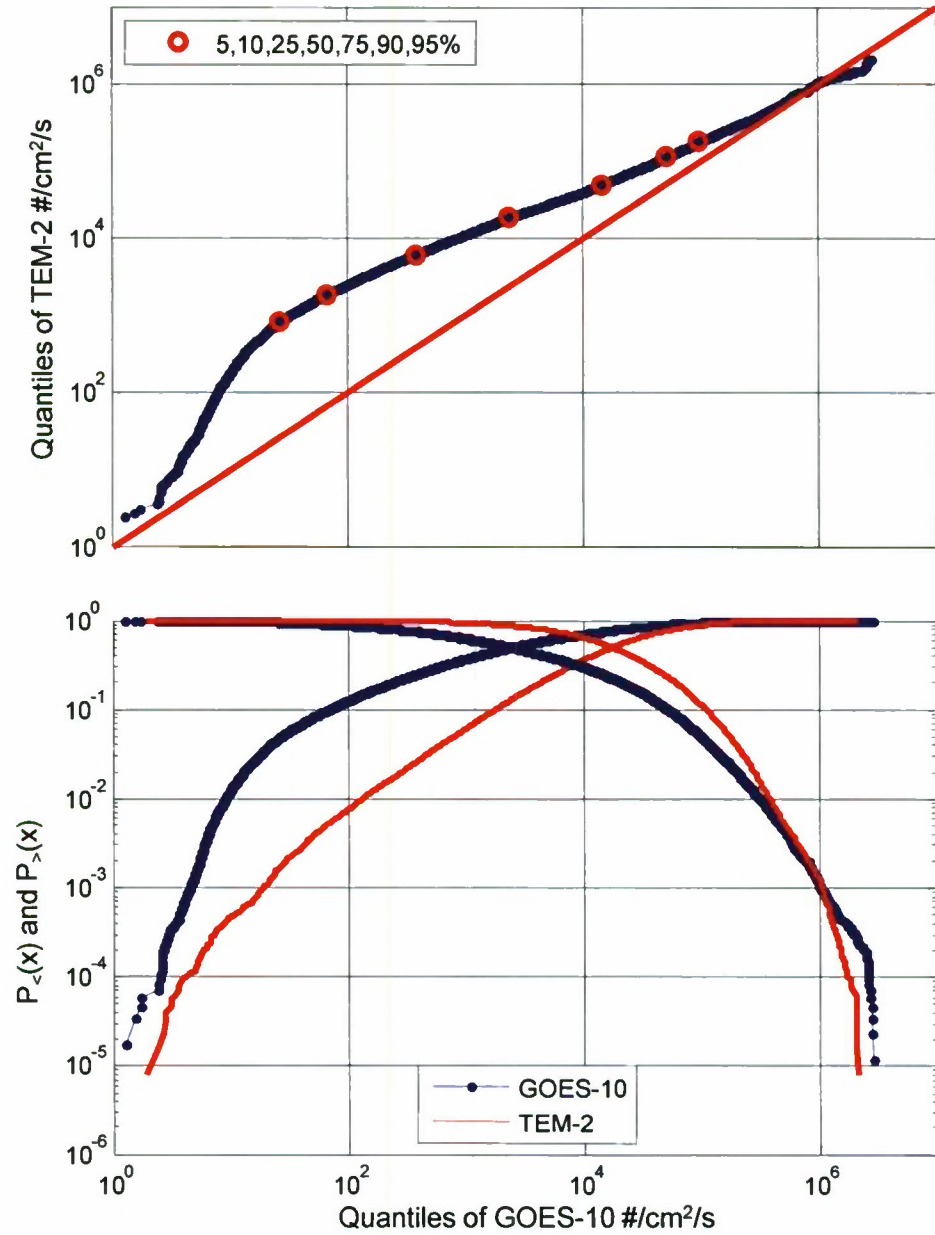


Figure 12: Comparison of TEM-2 scenarios and GOES-10 observed statistical distribution of > 2 MeV electron flux. The plot format follows that of Figure 1. GOES-10 flux is multiplied by 3π as in Figure 11. The TEM-2 distribution shown is taken from 200 Monte Carlo scenarios.

the figure are GEO-specific models, based on observations at GEO: IGE [Sicard-Piet *et al.*, 2008], Fennell *et al.* [2000], and O’Brien *et al.* [2007] worst case observed and flux limits. The primary curves of interest are the percentiles from 40 Monte Carlo scenarios in TEM-2. These curves represent the best estimate (median), and various confidence values from the Monte Carlo scenario method. For example, there is nominally a 5% chance that the average flux for any given 10 year mission will exceed the curve labeled “95% Monte Carlo.”

In both panels of Figure 13, for reference, TEM-2 curves are plotted for the static mean, median and/or 95th percentile. However, these curves do not necessarily represent realistic environments and are really only useful as diagnostics. Additionally, there is the comparable result at GEO from the TEM-2 reanalysis (see sections 3-5). The appropriate static CRRESELE model is also provided in each panel for comparison.

Finally, as shown in the top panel of Figure 13, for a “quick-and-dirty” calculation of the average flux, one can avoid the time-dependent scenario calculation, and fly the mission through a static “Perturbed Mean” for each scenario. This calculation is expedient because it only requires the perturbation of the flux map (41) for each scenario and a relatively small number of orbits through the average from that perturbed map, rather than performing the full mission-length calculation required for the Monte Carlo curves. However, the “Perturbed Mean” neglects the “weather” dynamics (38), and can give incorrect results for short missions. Further, the “Perturbed Mean” can not be used for quantities that are time-sequence dependent (e.g., a worst case 24-hour flux).

Several points are evident from Figure 13. First, it is obvious that TEM-2 is quantitatively different from AE8 and the other models. Given that TEM-2 used no GEO data, the obvious conclusion is that TEM-2 is likely inferior, at least to IGE and the Fennell/O’Brien models. We assume that in future models (i.e., AE9), GEO data will be included and agreement with these models will improve. Second, the spread from the median to the 95th percentile is only a factor of 2-4, which is consistent with the spread among the other models, where provided. However, the models do not always agree with each other within these error bars. Later models (i.e., AE9) promise improved treatment of the measurement errors, both including error estimates for each measurement and including more data sets. Finally, the worst case estimates, although in major disagreement with the Fennell and O’Brien models [Fennell *et al.*, 2000; O’Brien *et al.*, 2007], are nonetheless bounded by these models, except at very high energies (> 4 MeV).

2.3.2 GPS example

Figure 14 shows the same quantities as in Figure 13, except for a nominal GPS orbit. In place of the IGE model, we have used the MEO GNSS model, provided by ONERA [Sicard-Piet *et al.*, 2006; Bourdarie *et al.*, 2010]. For the average environment (top), quantitative agreement is surprisingly good. For the worst case environment (bottom), the only comparison is to CRRESELE Max. So, we cannot learn much about quantitative performance, but the local maxima evident in the percentiles of the Monte Carlo scenarios are very suspicious, and likely erroneous. Since they are absent from the static 95% environment, they are likely an artifact of either large measurement errors on specific sensors, or truncation of the principal components in the prior model.

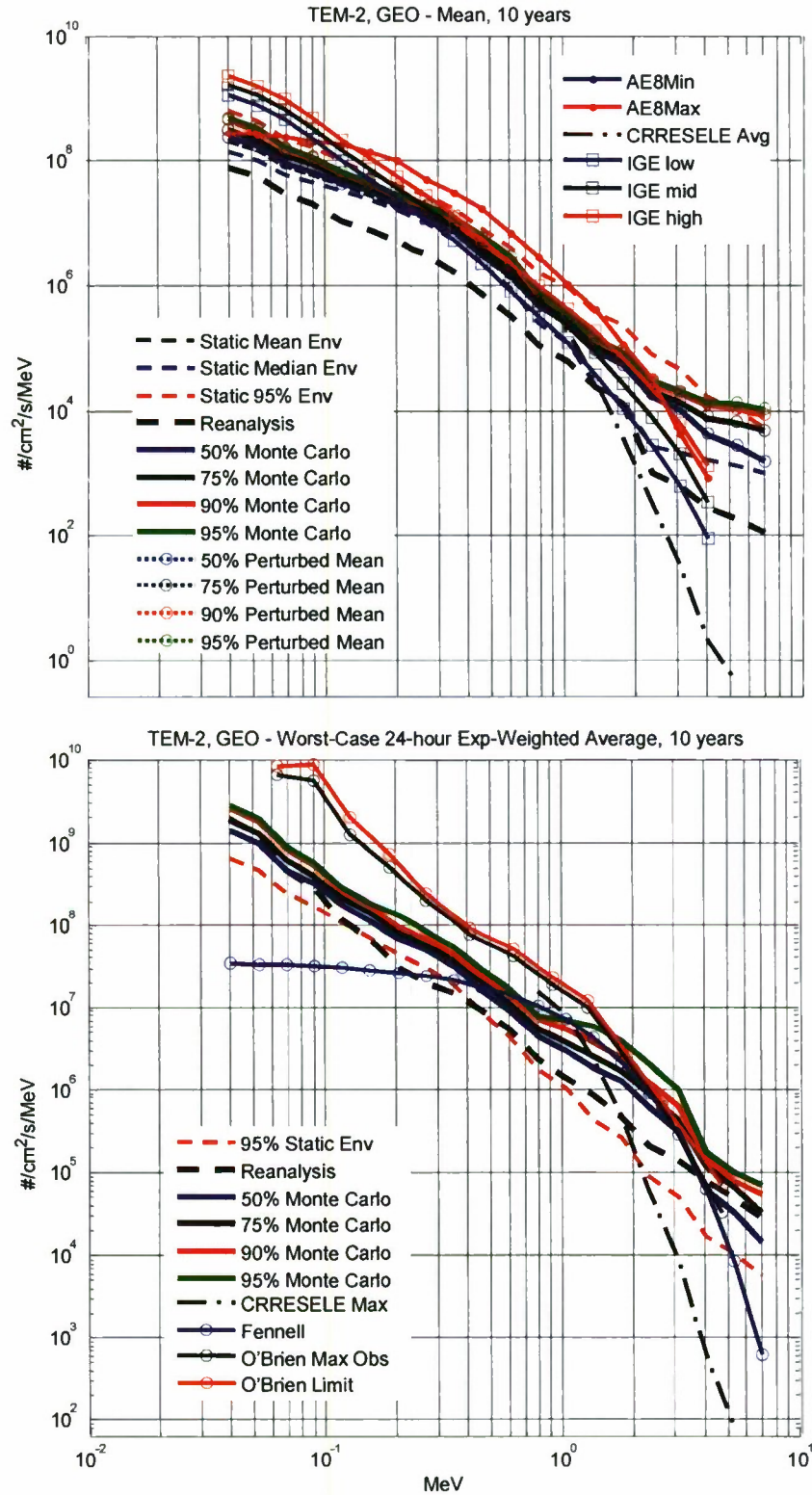


Figure 13: 10-year environments at GEO. Top: Mean flux from various models; AE8 (MIN and MAX are the same at GEO). Bottom: worst-case 24-hour exponentially-weighted flux average.

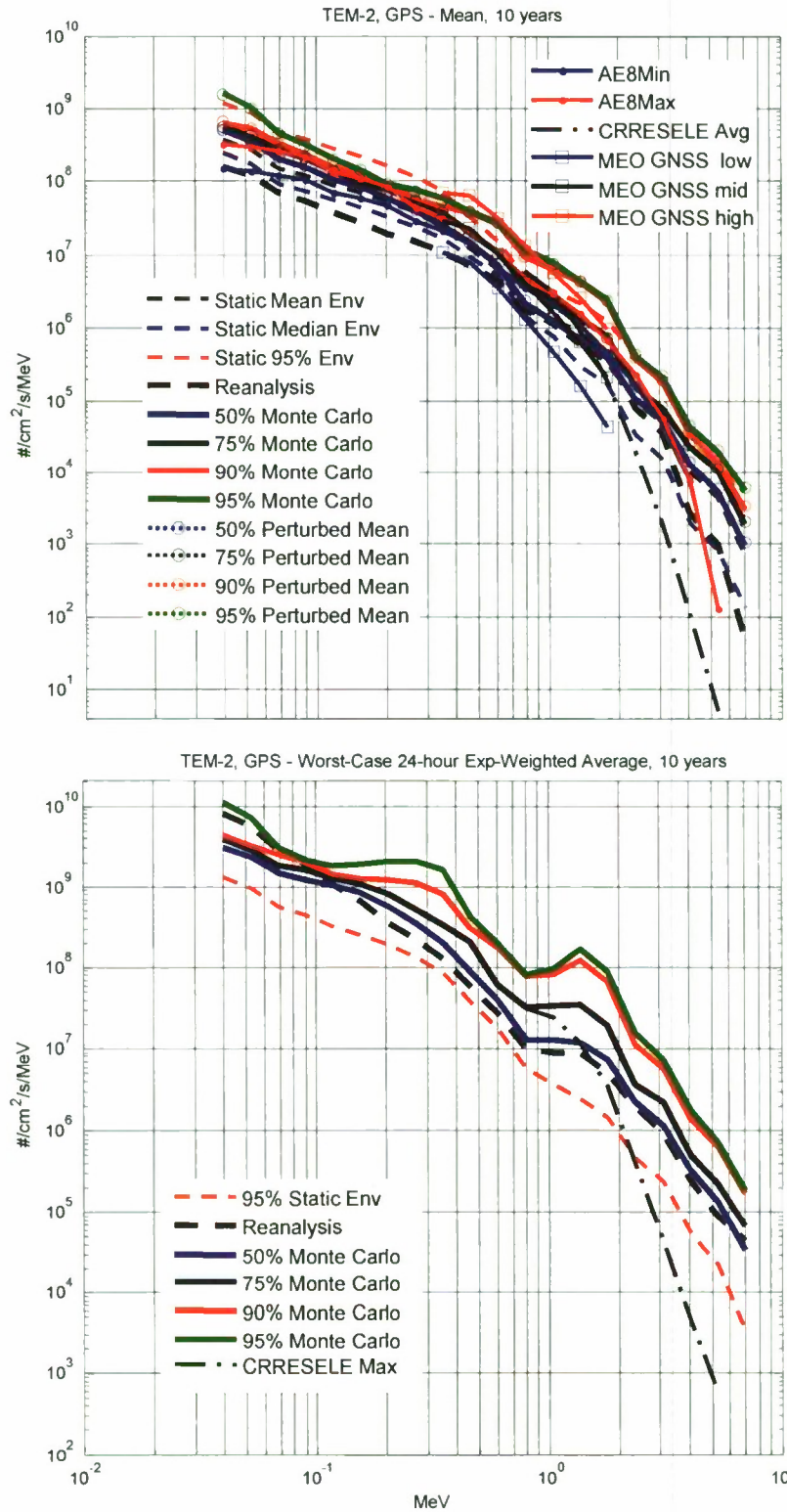


Figure 14: 10-year environments at GPS. Top: Mean flux from various models; AE8. Bottom: worst-case 24-hour exponentially-weighted flux average.

2.3.3 Dose depth curves

Finally, one of the most widely-requested quantities that current models cannot produce for an arbitrary orbit is “error bars on dose-depth curves.” Figure 15 shows just this quantity from TEM-2 for GEO (top) and GPS (bottom) orbits. For comparison, we have also plotted dose computed from reference mean environment models used in Figures 13 and 14. Again, quantitative agreement is poor, especially beyond 100 mils of Aluminum shielding. Nonetheless, TEM-2, along with TEM-1, represents the first class of global trapped radiation model that can compute dose “error bars” which have real probabilities associated with them, accounting for both environmental dynamics and measurement error. This is a major step toward truly usable “next generation radiation specifications.” However, much work obviously remains to be done before a model like TEM-2 can be used quantitatively for satellite design.

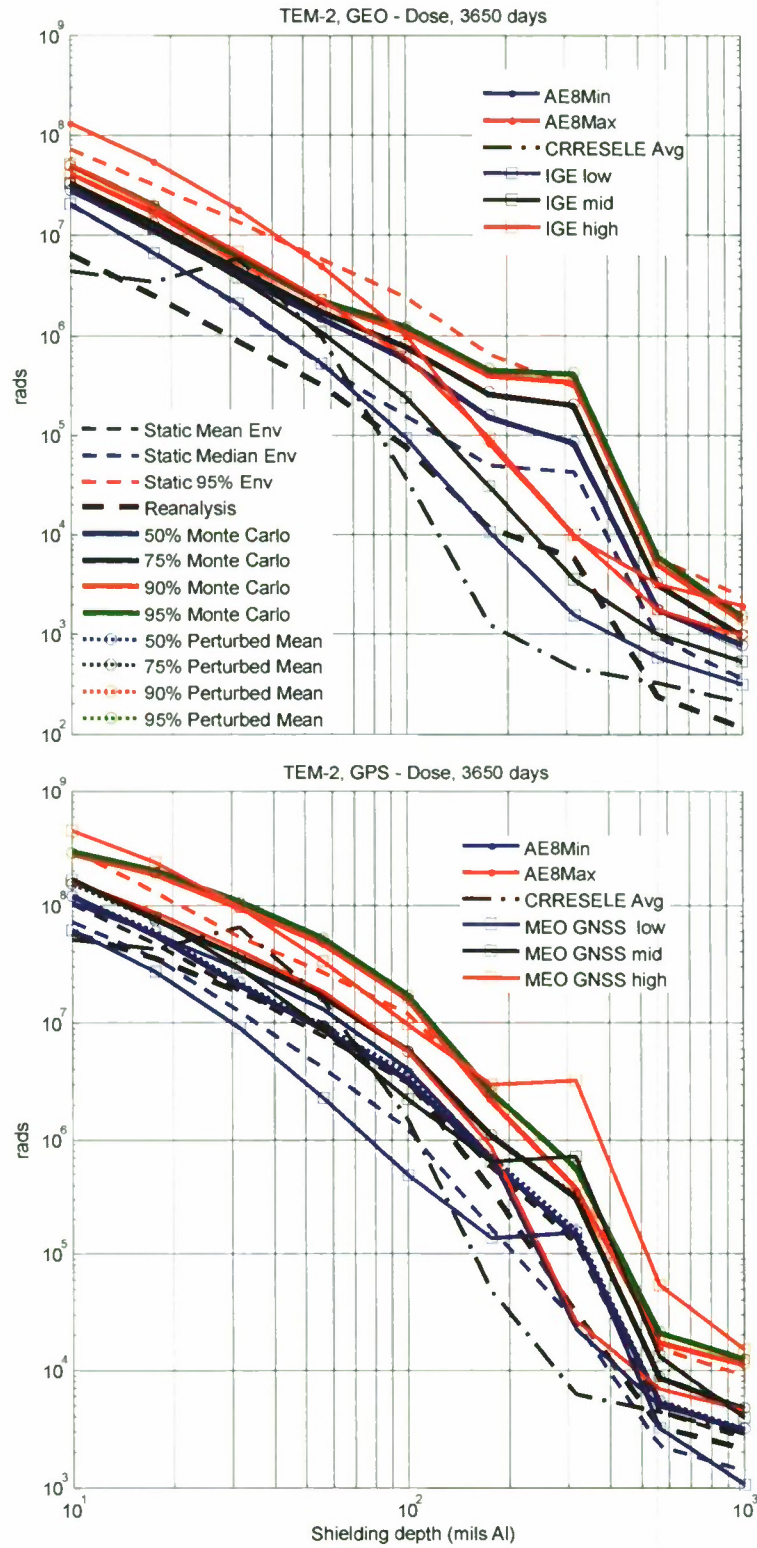


Figure 15: 10-year total dose environments at GEO (top) and GPS (bottom).

3 Reanalysis procedures

In addition to the engineering application demonstrated above, TEM-2 can also be used as the “background” model for a long-term reanalysis. We will discuss how the prior model is used with long-term observations of typically lower resolution to estimate the global state of the electron radiation belts in 6-hour snapshots over an entire solar cycle—a statistical reanalysis. Whereas data assimilation usually involves a maximum likelihood state that balances observational errors with the output of a global simulation, in the following demonstration, the statistical prior model from TEM-2 will stand in for the output of the physical simulation. We will also discuss the “cross-calibration” of the reanalysis data sets, and the validation of the reanalysis. Finally, we will discuss some potential scientific uses of our reanalysis.

3.1 Stating the data assimilation problem

The objective of our data assimilation is to obtain the most likely state of the electron belts given a set of observations taken near a fiducial time of interest. In an ideal situation, one would have a large set of observations \vec{y} of the phenomenon of interest \vec{x} (i.e., radiation belt fluxes on a global grid), and one could solve for \vec{x} by least squares or more sophisticated inversion methods. Formally,

$$\vec{y} = \vec{H}(\vec{x}), \quad (42)$$

where $H_i(\vec{x})$ is the “measurement function” for the i^{th} observation, y_i . In the case of the radiation belts, the observations are typically integrals over flux (or phase-space density) plus a background (b). Since integrals are linear operators, we can represent (42) as

$$\vec{y} = \vec{b} + \underline{H}\vec{x}. \quad (43)$$

A least-squares solution is tempting:

$$\vec{x} = (\underline{H}^T \underline{H})^{-1} \underline{H}^T (\vec{y} - \vec{b}). \quad (44)$$

However, \underline{H} is typically underdetermined (there are more x ’s than y ’s), so that $\underline{H}^T \underline{H}$ is singular. A somewhat more sophisticated solution employs the pseudo-inverse:

$$\vec{x} = \underline{H}^\dagger (\vec{y} - \vec{b}). \quad (45)$$

This solution at least exists; however it solves the underconstrained problem by minimizing the length of the unspecified portion of \vec{x} . That is, it assumes that where there is no measurement, there is no flux (or phase-space density). Obviously, this is not a physically reliable assumption. Something more is needed to estimate \vec{x} .

In the inversion of Energetic Neutral Atom (ENA) images, it is common to enforce a smoothing criterion [DeMajistre *et al.*, 2004; Perez *et al.*, 2004]. Smoothing appears to work well for ENAs, but probably would not work well in the radiation belt—our underlying measurements are fluxes along spacecraft trajectories, rather than global images. Instead, we employ a maximum-likelihood approach: we want to estimate the most likely instantaneous state of the electron radiation belts consistent with not only a set of observations but also a prior model of the likelihood of the various states of the belts.

We have elected to work with the natural logarithm of flux ($\log \vec{x}$) because flux errors are typically treated as multiplicative (e.g., the traditional “factor of 2”) rather than additive. Also, maximum

likelihood log flux provides more realistic solutions than maximum likelihood flux, because the mode (i.e., maximum likelihood value) of most flux distributions tends toward zero, and this is especially problematic in a multivariate flux distribution. The mode of the log flux distribution is close to its median, thereby representing a more “typical” value.

3.2 The likelihood to be maximized

Accepting that we will compute the maximum likelihood of $\log \vec{x}$ constrained to match a set of observations \vec{y} , in the usual notation of Bayesian conditional probabilities we want to find the value \vec{x} that maximizes:

$$\mathcal{L}(\log \vec{x}) = p(\log \vec{x} | \vec{y}) = \frac{p(\log \vec{x}, \vec{y})}{p(\vec{y})}. \quad (46)$$

Unfortunately, we do not usually know $p(\log \vec{x}, \vec{y})$ or $p(\vec{y})$. However, there are two quantities that we *can* obtain, from which we can compute enough of $p(\log \vec{x} | \vec{y})$ to find a maximum likelihood solution. Namely, we know the part of $\mathcal{L}(\log \vec{x})$ that depends on \vec{x} :

$$\begin{aligned} p(\log \vec{x} | \vec{y}) &= \frac{p(\log \vec{x}, \vec{y})}{p(\vec{y})}, \\ &= p(\vec{y} | \log \vec{x}) \frac{p(\log \vec{x})}{p(\vec{y})}, \\ &\propto p(\vec{y} | \log \vec{x}) p(\log \vec{x}). \end{aligned} \quad (47)$$

In the last expression, we have dropped the $p(\vec{y})$ factor because it is invariant with respect to \vec{x} . The two quantities that remain are $p(\vec{y} | \log \vec{x})$, which is the probability of a given set of measurements (\vec{y}) assuming we know the state of the electron belts (\vec{x}), and $p(\log \vec{x})$, which is our so-called “prior” model. We note that $p(\vec{y} | \log \vec{x}) = p(\vec{y} | \vec{x})$ because the condition on $\log \vec{x}$ is equivalent to the condition on \vec{x} .

As is usually the case, instead of actually maximizing $\mathcal{L}(\log \vec{x})$, we will minimize its negative logarithm (without the terms that are constant with respect to \vec{x}):

$$-\log \mathcal{L}(\log \vec{x}) \sim \ell(\log \vec{x}) = -\log p(\vec{y} | \log \vec{x}) - \log p(\log \vec{x}). \quad (48)$$

The error covariance matrix for the maximum likelihood $\log \vec{x}$ is approximated by

$$\underline{\underline{\Omega}} = \text{cov} \log \vec{x} = \begin{pmatrix} \ddots & & \\ \cdots & \frac{d^2 \ell}{d \log x_i d \log x_j} & \cdots \\ & \ddots & \end{pmatrix}^{-1}. \quad (49)$$

The standard error δx_i on x_i is given by:

$$\frac{\delta x_i}{x_i} \approx \sqrt{\Omega_{ii}}. \quad (50)$$

3.3 The statistical prior model as a likelihood function

We begin to construct the terms in the maximum likelihood problem (48) with the “prior” model, $p(\log \vec{x})$. We will start with $p(\vec{q})$ and work our way to $p(\log \vec{x})$. We know from section 2.2.8, that \vec{q} has

a multivariate Gaussian distribution:

$$p(\vec{q}) = \frac{\exp[-\vec{q}^T \vec{q}/2]}{(2\pi)^{N_q/2}} \quad (51)$$

In the following we will need the generic relationship that describes a multivariate change of variables in probability calculus:

$$p(\vec{v}) = p(\vec{w}) \left| \frac{d\vec{w}}{d\vec{v}} \right|, \quad (52)$$

where $|d\vec{w}/d\vec{v}|$ is the determinant of the Jacobian of the change of variables. Further, we will need the related expression for monotonically increasing univariate changes of variables

$$\frac{dw}{dv} = \frac{p(v)}{p(w)}. \quad (53)$$

Both of these expressions can be derived from the conservation of probability density, which is analogous to the conservation law that governs changes of variables in integrals or phase spaces.

Applying the conversion from \vec{q} to \vec{z} , we have:

$$p(\vec{z}) = \frac{\exp[-\vec{z}^T \underline{\underline{\Sigma}}^{-1} \vec{z}/2]}{\sqrt{|\underline{\underline{\Sigma}}|} (2\pi)^{N_z/2}}, \quad (54)$$

noting that $|\underline{\underline{\Sigma}}| = |Q|^2$ in the idealized case of a non-singular $\underline{\underline{\Sigma}}$.

Converting to \vec{x} , we have:

$$p(\vec{x}) = \frac{\exp[-\vec{z}^T \underline{\underline{\Sigma}}^{-1} \vec{z}/2]}{\sqrt{|\underline{\underline{\Sigma}}|} (2\pi)^{N_z/2}} \prod_i \frac{f_i(x_i)}{\phi(z_i)} \quad (55)$$

where f_i is the probability density function for x_i , and ϕ is the probability density function for a unit normal (standard Gaussian):

$$f_i(x_i) = \frac{\partial F_i}{\partial x_i}, \quad (56)$$

$$\phi(z) = \frac{\exp[-z^2/2]}{\sqrt{2\pi}} = \frac{\partial \Phi}{\partial z}. \quad (57)$$

Finally, converting to $\log \vec{x}$, we have:

$$p(\log \vec{x}) = \frac{\exp[-\vec{z}^T \underline{\underline{\Sigma}}^{-1} \vec{z}/2]}{\sqrt{|\underline{\underline{\Sigma}}|} (2\pi)^{N_z/2}} \prod_i \frac{x_i f_i(x_i)}{\phi(z_i)} \quad (58)$$

When we take the negative logarithm and replace $\vec{z}^T \underline{\underline{\Sigma}}^{-1} \vec{z}$ with $\vec{q}^T \vec{q}$, we have

$$\begin{aligned} -\log p(\log \vec{x}) &= -\sum_i [\log x_i + \log f_i(x_i)] \\ &\quad + \frac{1}{2}(\vec{q}^T \vec{q} - \vec{z}^T \vec{z}) + \text{constants}. \end{aligned} \quad (59)$$

We note that the transform from \vec{z} to \vec{q} is constant and linear, and therefore it does not modify the log-likelihood function, except by the addition of a constant, which drops out of the optimization.

For f_i following a Weibull distribution, we differentiate (11)

$$f(x; x_0, \gamma) = \frac{\gamma x^{\gamma-1}}{x_0^\gamma} \exp \left[- \left(\frac{x}{x_0} \right)^\gamma \right], \quad (60)$$

which leads to

$$\begin{aligned} -\log p(\log \vec{x}) &= -\sum_i [\gamma_i \log x_i - (x_i/x_{0,i})^{\gamma_i}] \\ &\quad + \frac{1}{2}(\vec{q}^T \vec{q} - \vec{z}^T \vec{z}) + \text{constants}. \end{aligned} \quad (61)$$

For f_i following a log-normal distribution (14), we have a remarkably simple result:

$$z_i = \frac{\log x_i - \mu_i}{\sigma_i}, \quad (62)$$

$$\frac{\partial z_i}{\partial x_i} = (x_i \sigma_i)^{-1}, \quad (63)$$

$$f_i(x_i) = \frac{1}{x_i \sigma_i} \phi \left(\frac{\log x_i - \mu_i}{\sigma_i} \right) = \frac{\phi(z_i)}{x_i \sigma_i}, \quad (64)$$

$$-\log p(\log \vec{x}) = \frac{1}{2} \vec{q}^T \vec{q} + \text{constants}. \quad (65)$$

Depending on our choice of marginal distribution, either (61) or (65) supplies $-\log p(\log \vec{x})$ in the maximum likelihood problem (48). In either case, the vector of medians occurs at $\vec{z} = 0$, which is also $\vec{q} = 0$, providing a reasonable starting point for the numerical optimization algorithm. The optimization will occur in \vec{q} , but will maximize the likelihood of $\log \vec{x}$.

In the reanalysis, we use a lognormal marginal distribution rather than the Weibull used in the rest of TEM-2. The Weibull tends to pull the reanalysis solution away from the data because the maximum likelihood log flux at some gridpoints is much higher than the median log flux. By using a lognormal, for which the maximum likelihood log flux is the median log flux, we effectively penalize deviations from the median, rather than from the maximum likelihood log flux.

3.4 The grid interpolation functions

In order to relate the radiation belt state (\vec{q} or \vec{x}) to observations (i.e., to compute $p(\vec{y} | \log \vec{x})$), we will need to interpolate between grid points. The flux x at any given E , α_{eq} , and L_m is given by the sum of a set of tri-linear finite elements:

$$x(E, \alpha_{eq}, L_m) = \sum_i x_i v_i(E, \alpha_{eq}, L_m). \quad (66)$$

Each element is the product of three linear contributions:

$$v_i(E, \alpha_{eq}, L_m) = v_i^{(E)}(E) v_i^{(\alpha)}(\alpha_{eq}) v_i^{(L)}(L_m), \quad (67)$$

and the linear contributions are defined as:

$$v_i^{(X)}(X) = \begin{cases} \frac{X - X_i^{\text{low}}}{X_i^{\text{mid}} - X_i^{\text{low}}} & X_i^{\text{low}} < X \leq X_i^{\text{mid}} \\ \frac{X_i^{\text{high}} - X}{X_i^{\text{high}} - X_i^{\text{mid}}} & X_i^{\text{mid}} \leq X < X_i^{\text{high}} \\ 0 & \text{otherwise} \end{cases}, \quad (68)$$

for X being either E , α_{eq} , or L_m .

The mid-point of one element is the high or low point of its neighbor, as would be expected. At the atmospheric boundary, the low point is set to the L_m -dependent analytical loss cone angle provided by (1), and no grid points exist inside the loss cone. The flux is zero beyond the mid-points of the grid points at the other boundaries of the grid.

3.5 Measurement functions

We consider a measurement to be an integration over time and velocity space. That integration will be discretized on our grid, and represented as a weighted sum over the model fluxes plus an expected background (b). Writing equation (43) in subscript notation, we have:

$$y_k \approx b_k + \sum_i H_{ki} x_i. \quad (69)$$

As we will see, the background can be estimated from other sensors on the vehicle. For the calculation of \underline{H} , we ignore temporal dependence over the duration of the measurement (T_k), and we represent velocity space in energy E and local pitch-angle α coordinates. Thus, the measurement function for observation y_k (in counts) taken at $(L_m, B/B_{eq})$ is given by:

$$H_{ki} = 2\pi T_k \int_{E_i^{\text{low}}}^{E_i^{\text{high}}} dE \int_{\alpha_1}^{\alpha_2} v_i(E, \alpha_{eq}(\alpha), L_m) A_k(E, \alpha) \sin \alpha d\alpha, \quad (70)$$

where $\alpha_{eq}(\alpha)$ relates equatorial and local pitch-angle via conservation of the first adiabatic invariant:

$$\frac{\sin^2 \alpha}{B} = \frac{\sin^2 \alpha_{eq}}{B_{eq}}. \quad (71)$$

The bounds of pitch-angle integration α_1 and α_2 are local pitch angles that correspond to either the low and high equatorial pitch angle limits of the grid point, or $\alpha_2 = \pi/2$, when the high equatorial pitch angle limit of the grid point includes locally mirroring particles. The function $A_k(E, \alpha)$ provides the instrument's effective area (in cm^2) for particles with energy E and local pitch-angle α . The units of H_{ki} are ($\text{cm}^2 \text{s keV}$). We have chosen to represent y_k as counts rather than counts-per-second or flux because the number of counts is a more accurate depiction of the usual measurement process, and it allows us to approximate the measurement error through a Poisson counting process when there are few counts. In our maximum likelihood treatment, we will use two error distributions, depending on whether Poisson counting error dominates instrument response uncertainty.

3.6 Pseudo-Poisson error distribution

If we assume that the k^{th} measurement is a Poisson process with expected counts λ_k , we have:

$$p(y_k | \lambda_k) = \mathcal{P}(y_k | \lambda_k) = \frac{\exp(-\lambda_k) \lambda_k^{y_k}}{y_k!}, \quad (72)$$

$$\lambda_k = b_k + \sum_i H_{ki} x_i. \quad (73)$$

We next introduce β_k , a variance inflation factor (see section 4.3), which will allow us to maintain the shape of the Poisson distribution while modifying its variance. We will do this when we must optimize (48) for a variety of data points that are not all taken simultaneously. We can preserve the maximum likelihood value of $p(y_k|\lambda_k)$ while inflating the variance by $1/\beta_k$ using the following transform:

$$p(y_k|\lambda_k; \beta_k) = \mathcal{P}(y_k|\beta_k|\lambda_k/\beta_k). \quad (74)$$

The negative log and gradient are given by:

$$\hat{\ell} = -\log p(y|\lambda; \beta) = \beta(\lambda - y \log \lambda) + \text{constants}, \quad (75)$$

$$\frac{\partial \hat{\ell}}{\partial \lambda} = \beta(1 - y/\lambda). \quad (76)$$

3.7 Gaussian error distribution

For most of our data, for sufficiently large counts, the predominant error source is our lack of knowledge of the true measurement function, $H(\vec{x})$. It is common to represent that uncertainty as relative error (δy), implying an approximately Gaussian distribution of the error in log counts or count rate.

The Gaussian error distribution for the natural log of y_k is:

$$\begin{aligned} p(y_k|\lambda_k; \delta y_k) &= \frac{\mathcal{G}(\log y_k | \log \lambda_k; \delta y_k)}{y_k}, \\ &= \frac{1}{\sqrt{2\pi} y_k \delta y_k} \exp \left[-\frac{1}{2} \left(\frac{y_k - \log \lambda_k}{\delta y_k} \right)^2 \right]. \end{aligned} \quad (77)$$

Again, we introduce a variance inflation factor β_k , which appears simply as

$$p(y_k|\lambda_k; \delta y_k, \beta_k) = \frac{\mathcal{G}(\log y_k | \log \lambda_k; \delta y_k/\sqrt{\beta_k})}{y_k}. \quad (78)$$

The negative log and gradient are given by:

$$\begin{aligned} \hat{\ell} &= -\log p(y|\lambda; \delta y, \beta) \\ &= \frac{1}{2} \left(\frac{\log y - \log \lambda}{\delta y} \right)^2 \beta + \text{constants}, \end{aligned} \quad (79)$$

$$\frac{\partial \hat{\ell}}{\partial \lambda} = \frac{\log \lambda - \log y}{\delta y^2 \lambda} \beta. \quad (80)$$

Table 3: Data channels used to drive the reanalysis

Channel	Sensor Type	Energy	δy
HEO-1, 1994-2008, $L > 4$			
E1	Telescope	>0.13 MeV	1.4
E2	Telescope	>0.23 MeV	1.2
E3	Dosimeter	>1.5 MeV	1.2
E4	Dosimeter	>4.0 MeV	1.1
E5	Dosimeter	>6.5 MeV	1.4
E6	Dosimeter	>8.5 MeV	1.1
HEO-3, 1997-2008, $L > 2$			
E3	Telescope	>0.45 MeV	1.5
E5	Dosimeter	>1.5 MeV	1.3
E6	Dosimeter	>3.0 MeV	1.3
ICO, 2001-2008, $L > 2.5$			
E1	Dosimeter	>0.95 MeV	0.93
E2	Dosimeter	>2.0 MeV	1.0
E3	Dosimeter	>3.5 MeV	0.97
E4	Dosimeter	>5.5 MeV	0.79
E5	Dosimeter	>6.8 MeV	0.81
SAMPEX, 1992-2004, all L			
PET/ELO	Telescope	2-6 MeV	*

* see section 4.2

4 Reanalysis data

For the reanalysis, we rely primarily on a combination of simple sensors developed by The Aerospace Corporation and known as HEO-1, HEO-3, and ICO. Each of these sensors can be thought of as an approximately omnidirectional integral electron channel. The HEO vehicles are in 12-hour, critically inclined, Molniya orbits, giving them access to $L_m \sim 2$ at the magnetic equator and higher L shells at higher magnetic latitudes. The HEO-1 vehicle only telemeters data for $L_m > \sim 4$. The ICO vehicle (2001-026) is in a circular orbit, at $\sim 10,390$ km, with an inclination of 45° , crossing the magnetic equator at $L_m \sim 2.5$.

Finally, to provide some indication of the variation of inner zone electrons, we utilize the SAMPEX PET/ELO “L bin” history provided by S. Kanekal (private communication), from 1992-2004. SAMPEX is in a circular ~ 600 km orbit at 82° inclination. In section (4.2), we will discuss how this satellite that is primarily in the loss cone is used to constrain the trapped population.

4.1 HEO and ICO data

Both HEO-1 and HEO-3 carry simple, two-element solid-state telescopes (E1 and E2 in Table 3). However, on HEO-3, these channels are unusable for years at a time due to what appears to be a thermal background. Further, HEO-3 carries an additional telescope, E3, with minimal collimation. The attitude information for these vehicles is not available, so the telescopes are treated as omnidirectional sensors. Both HEO vehicles and ICO carry dosimeters, consisting of a silicone target behind a dome shield. Each dosimeter has a unique dome, to distinguish incident particle energy, and

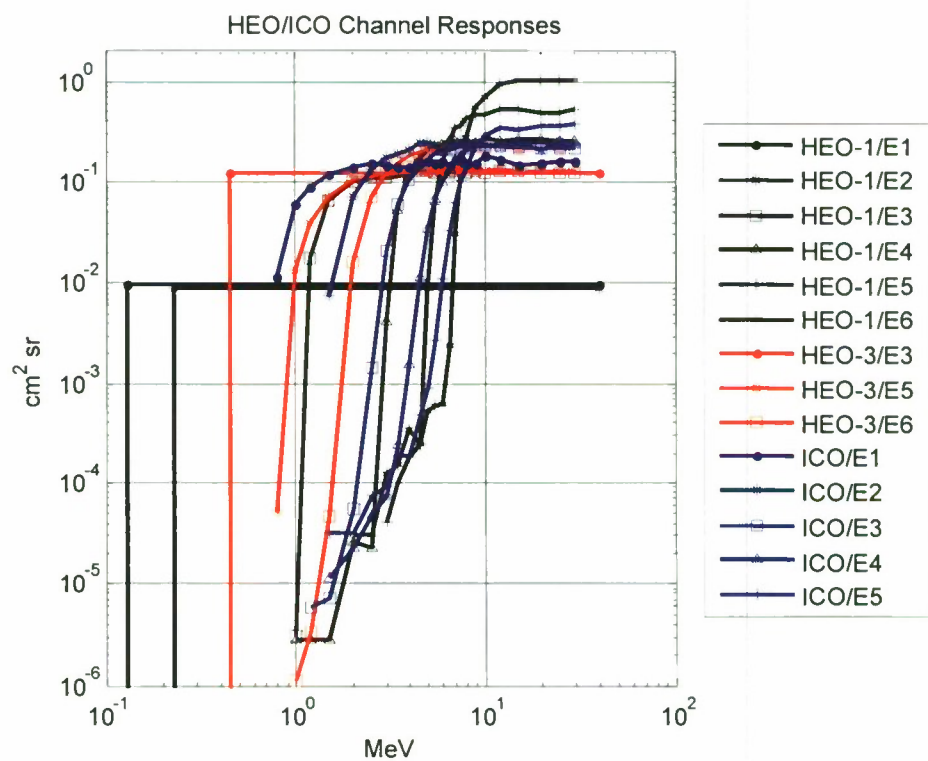


Figure 16: Calculated energy response curves for HEO and ICO channels.

analysis of the energy deposited in the silicon target provides rudimentary differentiation between protons and electrons. For each “electron” channel, there is a corresponding “proton” channel that is used to estimate the channel’s background. Before being used in the reanalysis, the HEO and ICO data are binned into $0.25 L_m$ bins using the OPQ magnetic field model.

Although we have not formally intercalibrated the HEO and ICO data, we did perform some preliminary corrections based on the observed response to galactic cosmic rays when the vehicles are outside the radiation belts. This led to some constraint on the relative geometric factors of the sensors. Further, we used early iterations of the reanalysis to correct for some apparent systematic errors in the channel response. For example, if, in sample, the reanalysis solution was systematically lower than the observed counts in a particular channel, we assumed that channel’s response function needed to be rescaled upward.

As for the background, a simple scatter plot of each dosimeter electron channel to its corresponding proton channel (not shown) reveals a linear cutoff for lowest electron count rate as a function of the proton count rate. By assuming (safely) that this cutoff represented the case where the proton background dominated the electron signal, we were able to determine a simple scale factor (a multiplier of $\sim 2 - 3$) converted the count rate in each proton channel into a proxy background for its corresponding electron channel.

4.2 SAMPEX data

Data from SAMPEX is somewhat problematic because it is nearly always in the loss cone. However, large-scale global correlations [Kanekal *et al.*, 2001] in the electron belts suggest that such a sensor can nonetheless provide valuable information about the gross behavior of the otherwise-unobserved inner belt electrons. To utilize the SAMPEX data we relate it to the HEO3/E5 (> 1.5 MeV) channel for the high altitude legs of the HEO-3 orbit. For each $0.1 L_m$ from 3 to 8, we obtain power-law regression parameters between SAMPEX PET/ELO [Cook *et al.*, 1993] and HEO3/E5 based on daily averages. In addition to the power-law parameters, we compute the typical B/B_{eq} value of the HEO3/E5 data, and we compute an RMS error in the log fluxes, which serves as δy . Figure 17 shows the L_m dependence of these parameters. For $L_m < 3$, where the power-law regression breaks down, we use the regression values for $L_m = 3$, but multiply δy by 3, to produce only qualitative influence over the inner zone. The background is assumed to be 0, and a Gaussian relative error distribution is used.

4.3 Accounting for latent data

In order to make the reanalysis robust to data gaps, we include data outside the nominal time window for a particular fiducial time. That is, the fiducial cadence is 6 hours, but we include data from a larger window. The minimum time window includes 2 whole passes through the radiation belt. However, in case of a data gap, the window is expanded in either or both directions in time to allow at least one full pass before and one after the fiducial time.

To degrade the influence of data that is farther in the past or future, we need to know how the autocorrelation scales with time offset. In Figure 18, we have calculated the rank order correlation coefficient (Spearman’s ρ) between electron fluxes in each HEO-3 channel and their counterparts 1 day later (same orbit leg and odd/even parity). We see that there is very little dependence on energy or

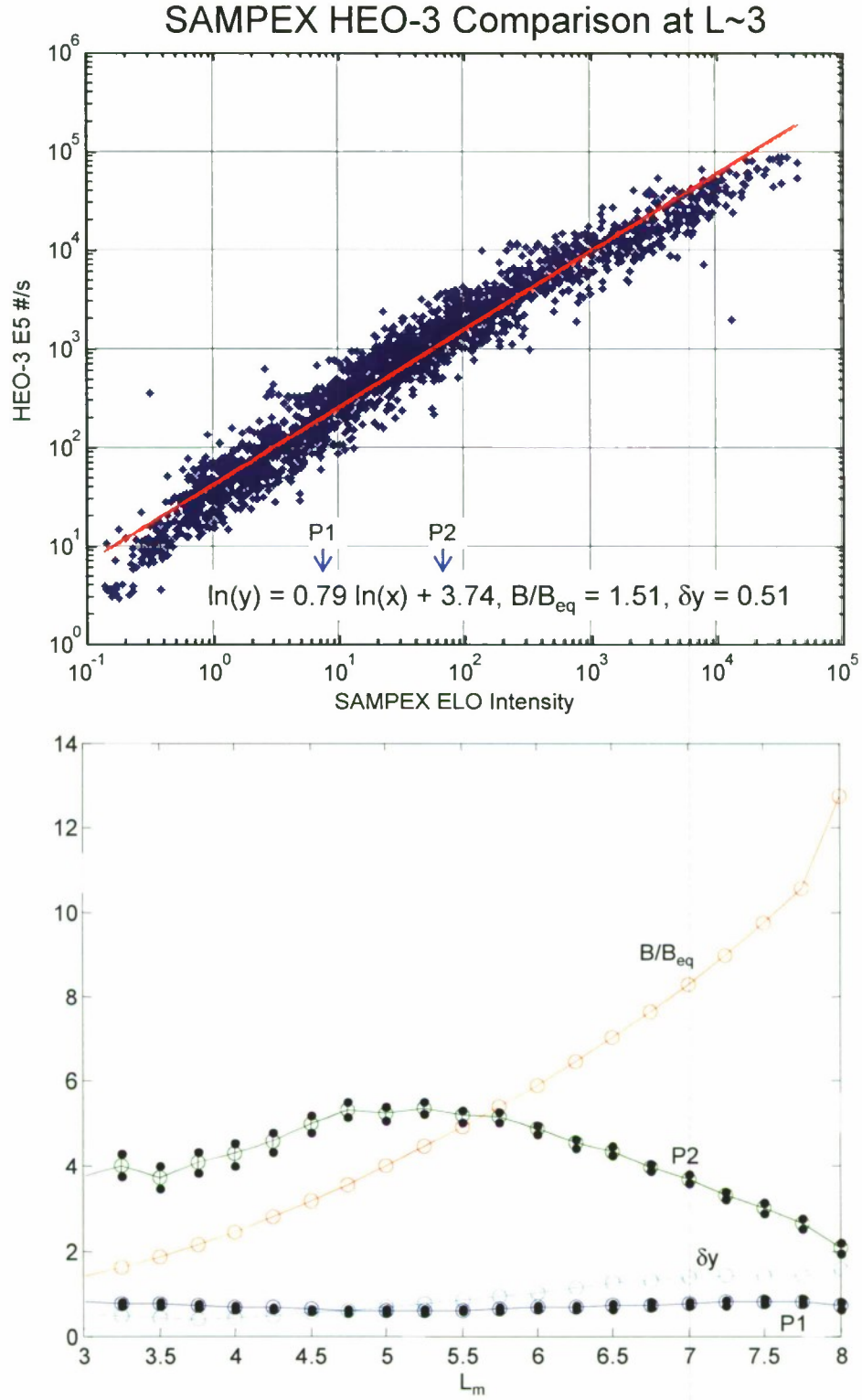


Figure 17: (Top) SAMPEX PET/ELO intensity can be used as a proxy for HEO-3 E5. (Bottom) The parameters of the proxy relationship vary with L shell.

Table 4: Coefficients for 1-day autocorrelation function vs L for HEO-3 fluxes

$r_{24,1}$	0.504938
$r_{24,2}$	0.477943
$r_{24,3}$	1.130208
$r_{24,4}$	4.254812

orbit status, at least at the higher energies. The correlation coefficient can be fit using the function:

$$r_{24}(L) = r_{24,1} + r_{24,2} \exp \left[- \left(\frac{L - r_{24,3}}{r_{24,4}} \right)^4 \right], \quad (81)$$

where the coefficients are given in Table 4.

Figure 19 shows that the correlation at 2 days is well modeled by the square of the correlation at 1 day. This is consistent with a first-order autoregressive process with correlation at arbitrary time difference Δt (in days) given by:

$$r_{\text{HEO}}(L, \Delta t) \sim r_{24}(L)^{|\Delta t|} \quad (82)$$

With a definition of how the autocorrelation varies with time offset, we can define the variance inflation factor β_k for measurement y_k :

$$\beta_k = r_{\text{HEO}}^2(L_k, \Delta t_k). \quad (83)$$

This β_k is used in the measurement penalty functions given in sections 3.6 and 3.7. Comparing to equations (75) and (79), we see that β is a linear multiplier on the likelihood function. Therefore, as the correlation goes to zero with increasing time offset, the effect of the measurement in the overall likelihood function goes to zero also.

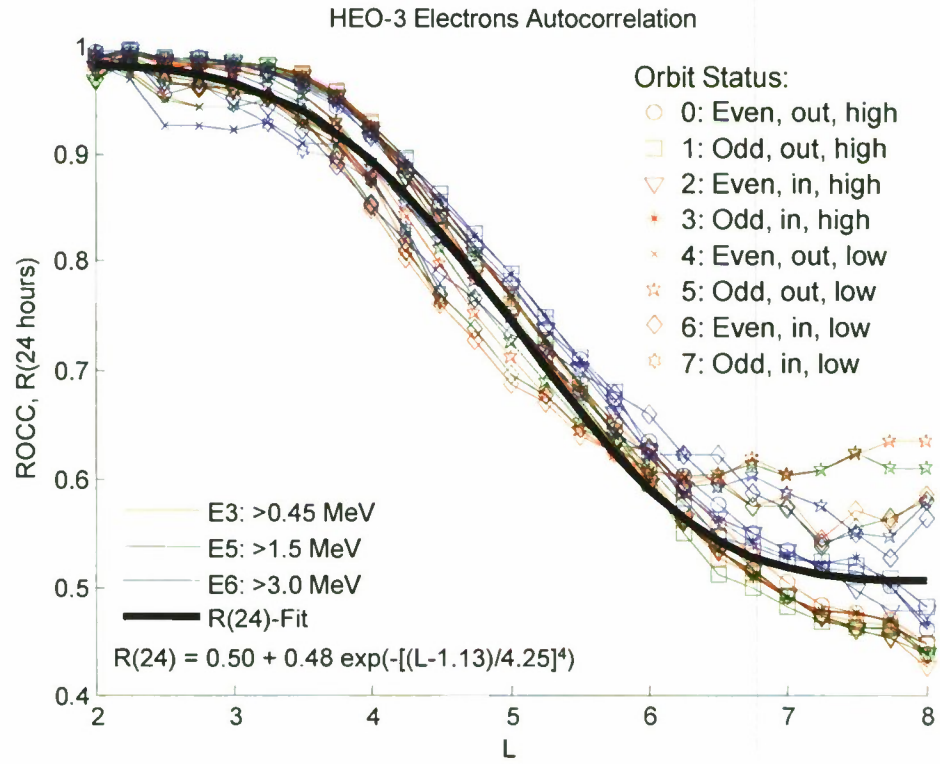


Figure 18: Autocorrelation for HEO-3 electron fluxes at 1 day lag for all orbit status and energy channels.

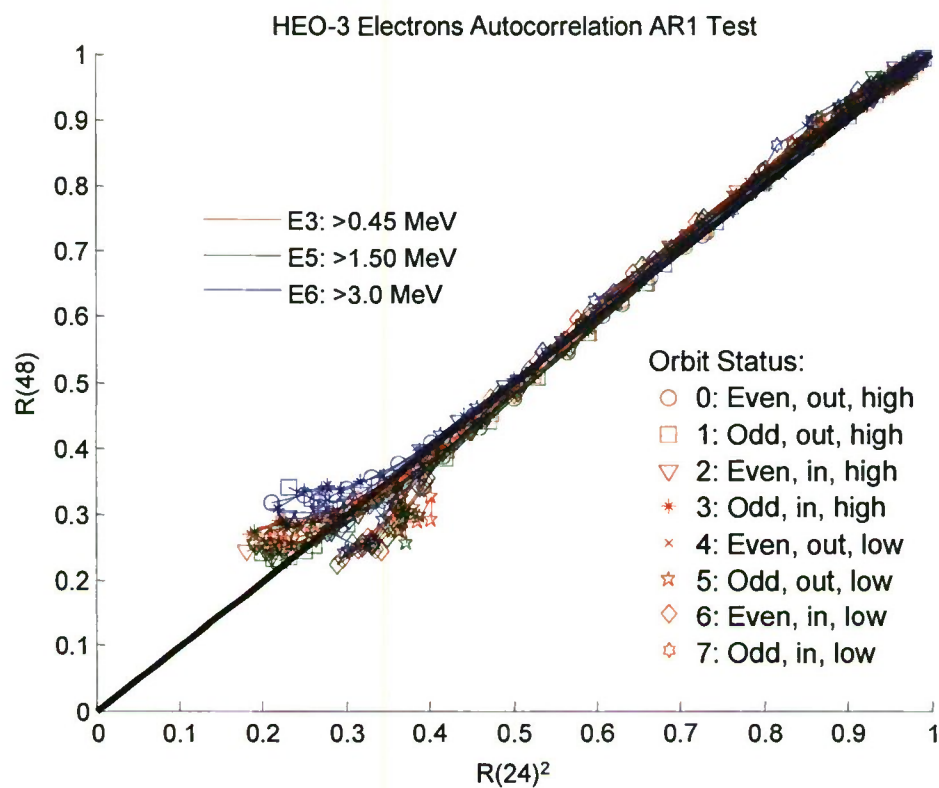


Figure 19: Autocorrelation for HEO-3 electron fluxes at 2 days lag versus the square of the correlation at 1 day lag for all orbit status and energy channels. The good agreement suggests that the HEO-3 autocorrelation is a first-order autoregressive process.

Table 5: ICO out-of-sample validation statistics

Channel	$\langle \log_{10}(y/\lambda) \rangle$	$\langle \log_{10} y/\lambda \rangle$	RMSE($\log_{10} y, \log_{10} \lambda$)	PE %	std $\log_{10} y$
E1	0.410	0.572	0.771	74.1	1.515
E2	0.490	0.628	0.816	72.5	1.556
E3	0.297	0.633	0.789	69.0	1.417
E4	0.048	0.479	0.612	66.4	1.055
E5	0.071	0.339	0.436	73.8	0.853

5 Reanalysis results

We performed the reanalysis process for every 6 hour time step from 1992-2008. Figure 20 shows the entire interval, and two shorter sub-intervals. One can see that there are dynamics in all three regions of the electron belts: inner belt evolution (driven by SAMPEX data), slot filling and emptying, and outer zone dynamics. The progressive filling and emptying of the slot, in particular, is striking. One can also observe several occasions when the inner edge of the outer zone retreats to higher L during magnetically quiet periods. These phenomena are fairly well known, so their presence is reassuring.

5.1 Validation and known issues

To validate the reanalysis results, we have performed the reanalysis procedure on a shorter interval (2002 and 2003) without ICO data. We can then reconstruct what ICO would have seen in that reanalysis and compare with observations. Figure 21 shows several comparisons of ICO observations (y) to the reanalysis (λ) in counts. In the top left panel, we see in-sample validation: when ICO data is used in the reanalysis, how well does the optimized flux map reproduce the ICO data? We see that even in sample, the presence of other data sets pulls the solution away from the ICO data to some extent, especially at higher L_m where the magnetic coordinates are least reliable. The other panels of Figure 21 show out-of-sample comparisons for each ICO data channel. The lower-energy channels (E1, E2) show noticeable overestimates in the reanalysis for $L_m \sim 5 - 6$. One explanation for this disagreement could be the reduced performance at high L_m of the magnetic coordinates we have chosen, and another explanation could be incomplete intercalibration of the IIEO and ICO data.

Quantitatively, we can compare the observed (y) and estimated (λ) ICO counts in a number of ways. Table 5 provides out-of-sample validation statistics for each ICO channel. The $\langle \rangle$ operator defines a sample average, and PE stands for prediction efficiency, which is the ratio of the mean squared error between $\log_{10} y$ and $\log_{10} \lambda$ to the variance of $\log_{10} y$ subtracted from one, expressed as a percentage. The final column provides, for reference, std $\log_{10} y$, the standard deviation of $\log_{10} y$. The performance, in terms of prediction efficiency, is comparable across all channels. The mean absolute error (column 3) and the root mean squared error (RMSE) (column 4) correspond to multiplicative errors on the order of a factor of 2. The fact that the mean error in column 2 is not zero suggests that λ is systematically higher than y , by 30%-50% for E1-E3, but by less than 10% for E4 and E5. These systematic errors suggest incomplete intercalibration.

A more detailed survey of other energies and pitch angles, besides what is shown in Figure 20, reveals some expected shortcomings of the reanalysis. The reanalysis exhibits poor performance when no bounding data are available; e.g., in the inner zone away from 1.5 MeV or in the outer zone before HEO-3 data begins. Further, since the constraint data are nominally omnidirectional integral channels,

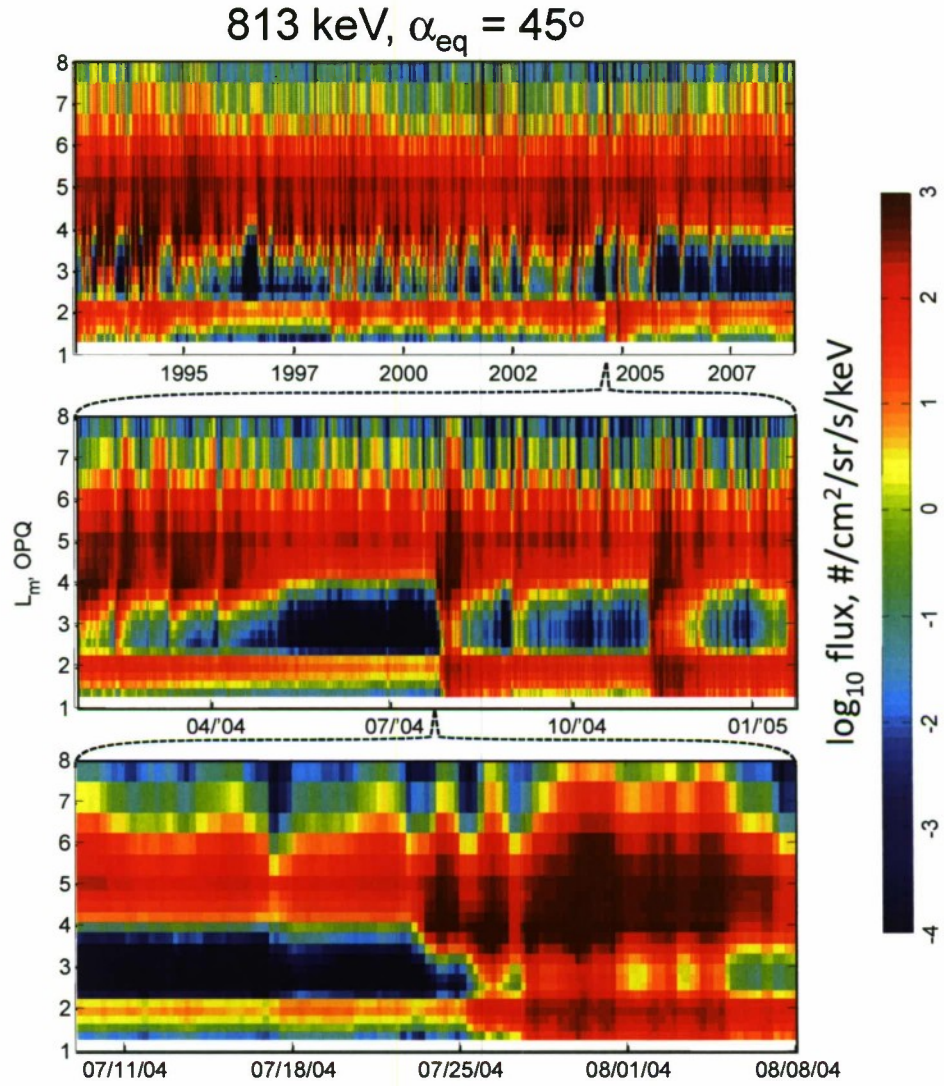


Figure 20: Flux versus L_m profiles versus time in the TEM-2 Reanalysis: (top) the entire reanalysis, (middle) one year, centered on the July 2004 storm, and (bottom) one month centered on July 24, 2004.

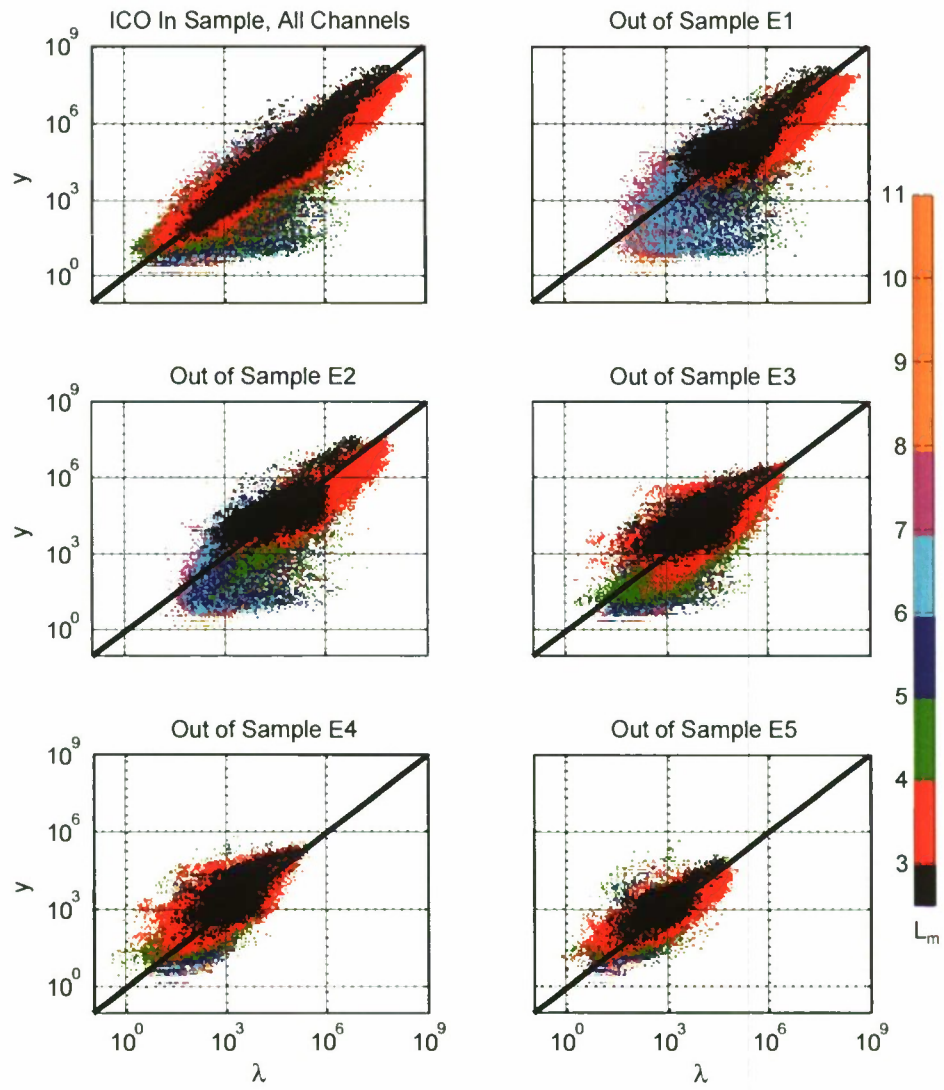


Figure 21: Validation of TEM-2 reanalysis versus ICO (in and out of sample).

the reanalysis sometimes produces unphysical or at least suspicious differential energy spectra and angular distributions. This problem likely stems primarily from a lack of intercalibration, but it also is compounded by our choice of magnetic coordinates (i.e., bounce rather than drift invariants and a quiet rather than active magnetic field model).

5.2 Engineering application

With appropriate caution, we can move on to apply the reanalysis results to engineering applications. Figures 11, 13, 14, and 15 all include a trace for the TEM-2 reanalysis. While the reanalysis shows generally poor quantitative performance (possibly due only to intercalibration), it often shows qualitative agreement. In particular, the reanalysis in Figure 11 captures some of the sharp increase in flux at GOES on March 18-20, 2006. The dynamics in the reanalysis represent real events with more-or-less complete temporal correlations (rather than the first order temporal behavior represented statistically in the Monte Carlo scenarios). This potentially very realistic environmental dynamics could be used to characterize idiosyncratic effects of individual storms. The Monte Carlo scenarios and the static models have no hope of representing that type of idiosyncratic behavior. It remains to be seen whether a more quantitatively accurate reanalysis model will be able to reproduce the worst cases, since the nonlinear optimization (48) tends to suppress extreme values.

5.3 Science application

The reanalysis simplifies the use of standard tools developed for particle measurements, and, as we will see, it enables use of some uniquely global tools. The reanalysis allows one to pick a particular energy, equatorial pitch angle, and L_m value and examine only the temporal variation of flux or phase-space density; or, one can select a slice along one or more of the dimensions to perform multivariate time series analysis, without having to explicitly account for the orbital motion of the observatories or data gaps in one or another sensor data set. However, as we will see, reanalysis also allows one to do things that were never before possible.

5.3.1 Empirical determination of the time evolution operator

Space physicists usually assume that the phase space density f_t (a continuous function of one or more adiabatic invariants) evolves according to a linear operator (usually diffusion):

$$\dot{f}_t = \hat{D}_t f_t + S_t, \quad (84)$$

where \dot{f}_t is a time derivative, \hat{D}_t is a time-varying linear operator, and S_t is a time-varying combined additive source and loss term. If one assumes that \hat{D}_t is constant at \bar{D}_T among a set of times T , e.g., all times when the magnetic index Kp is in some narrow range, then one can actually estimate \bar{D}_T from a multivariate sample of f_t for $t \in T$.

First, one discretizes f_t to \vec{f}_t , with time step Δt , giving a matrix-vector time evolution equation:

$$\begin{aligned} \vec{f}_{t+1} &= \vec{f}_t + \Delta t \left(\underline{D}_t \vec{f}_t + \vec{S}_t \right), \\ &= \left(\underline{I} + \Delta t \underline{D}_t \right) \vec{f}_t + \Delta t \vec{S}_t. \end{aligned} \quad (85)$$

Then, for $t \in \mathcal{T}$, one removes the average density and computes sample correlations:

$$\vec{g}_t = \vec{f}_t - \langle \vec{f}_t \rangle_{\mathcal{T}}, \quad (86)$$

$$\underline{\underline{\Sigma}}_{\mathcal{T}} = \langle \vec{g}_t \vec{g}_t^T \rangle_{\mathcal{T}}, \quad (87)$$

$$\underline{\underline{R}}_{\mathcal{T}} = \langle \vec{g}_t \vec{g}_{t+1}^T \rangle_{\mathcal{T}}. \quad (88)$$

We have made the very safe assumption that $\langle \vec{f}_{t+1} \rangle_{\mathcal{T}} = \langle \vec{f}_t \rangle_{\mathcal{T}}$.

One then subtracts $\langle \vec{f}_t \rangle_{\mathcal{T}}$ from both sides of (85), multiplies the result by \vec{g}_t^T , and takes the sample average over $t \in \mathcal{T}$, giving:

$$\langle \vec{g}_{t+1} \vec{g}_t^T \rangle_{\mathcal{T}} = \left(\underline{\underline{I}} + \Delta t \underline{\underline{D}}_{\mathcal{T}} \right) \langle \vec{g}_t \vec{g}_t^T \rangle_{\mathcal{T}} + \left\langle \left(\Delta t \vec{S}_t - \langle \vec{f}_t \rangle_{\mathcal{T}} \right) \vec{g}_t^T \right\rangle_{\mathcal{T}}. \quad (89)$$

Next, we assume that \vec{S}_t is uncorrelated with \vec{f}_t , i.e., that additive sources and losses are uncorrelated with phase space density. This is a reasonable, but not guaranteed, assumption, as most descriptions of losses in the literature are *multiplicative* (e.g., f_t/τ decay terms), and most additive source terms are actually parameterizations of linear processes operating on parts of f outside the simulation domain (e.g., a source due to stochastic diffusion from lower energies). In principle, the former can be addressed by incorporating $1/\tau$ into \hat{D} , and the latter can be addressed by expanding the simulation domain, or by assuming that the additive source is constant over the times identified by \mathcal{T} (e.g., the source is also parameterized with Kp , and would be represented by a constant $\vec{S}_{\mathcal{T}}$). Therefore the last term on the right is assumed to be zero, leaving:

$$\underline{\underline{R}}_{\mathcal{T}}^T = \left(\underline{\underline{I}} + \Delta t \underline{\underline{D}}_{\mathcal{T}} \right) \underline{\underline{\Sigma}}_{\mathcal{T}} + 0, \quad (90)$$

$$\underline{\underline{D}}_{\mathcal{T}} = \left(\underline{\underline{R}}_{\mathcal{T}}^T \underline{\underline{\Sigma}}_{\mathcal{T}}^{-1} - \underline{\underline{I}} \right) \frac{1}{\Delta t}. \quad (91)$$

In this formulation, \hat{D} need not be a diffusion operator. However, if it is, then $\underline{\underline{D}}_{\mathcal{T}}$ strongly constrains the diffusion coefficient, which can be estimated directly from its eigenvectors [see, e.g., *Schulz and Lanzerotti, 1974, section V.3, Spatial Quadrature*]. In any case, one can imagine obtaining $\underline{\underline{D}}_{\mathcal{T}}$ and $\vec{S}_{\mathcal{T}}$ for each value of Kp or some other index, and thereby obtaining a purely empirical model of the time evolution of the radiation belts.

5.3.2 Posterior principal component analysis

Another analysis technique that is possible only with the global time-varying specification provided by a reanalysis is principal component analysis. Whereas in 2.2.8 we used principal components (PCs) to resolve the problem of the singular spatial covariance matrix, we will here define a set of posterior principal components, which are the eigenvectors of the spatial covariance matrix of the log fluxes. As it happens, the covariance of log flux is invariant to the choice of flux or phase space density. The eigenvectors are not invariant to the choice of a grid. The grid we use for TEM-2 (section 2) approximately reflects our intuitive sense of where the information lies in the radiation belts: it is uniform in equatorial pitch angle, logarithmic in energy, and uneven in L_m . The L_m dimension has higher density at low L_m , and its midpoint in the L_m dimension is 3.75, roughly at the inner edge of the outer zone; therefore, the TEM-2 grid gives approximately as many grid points to the inner zone and slot as it does to the outer zone.

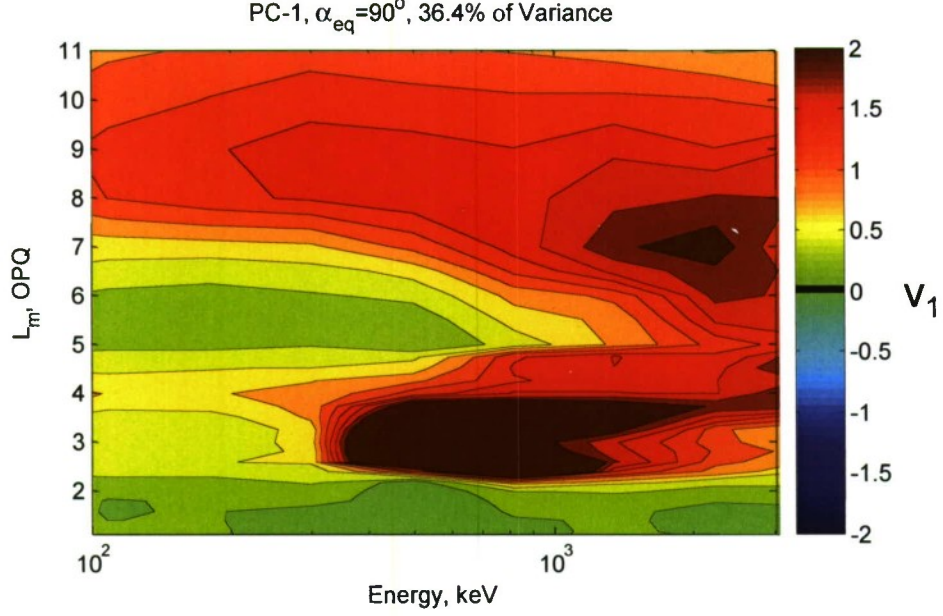


Figure 22: The first posterior principal component of the TEM-2 reanalysis, for equatorially mirroring electrons.

The posterior principal components we obtain are individually normalized to have a Pythagorean length corresponding to the number of variables in the “reduced” grid, and all have an arbitrary sign which we set to positively correlate with solar wind velocity (see below). The associated eigenvalue provides the amount of relative variance (in \log_{10} flux) described by each component. We then normalize the eigenvalues to sum to unity, and express them each as a percentage.

Figure 22 shows the first posterior principal component (PC-1) for equatorially mirroring electrons. As is often the case, the first PC has nearly all entries of the same sign and reflects the global coherence reported by *Kanekal et al.* [2001]. In this case, global coherence explains 36.4% of all the observed variance. Global coherence is likely associated with the *Dst* effect [e.g., *Kim and Chan*, 1997], an adiabatic effect not represented in our quiet field model (OPQ), and likely also with plasma-wave particle interactions that can span a large L_m range simultaneously. Specifically, losses associated with storm-time chorus and electromagnetic ion-cyclotron waves can act on all L_m values beyond the plasmapause [*Millan and Thorne*, 2007; *Shprits et al.*, 2008b]. During a magnetic storm, the plasmasphere is often eroded to very low L_m values [e.g., *Moldwin et al.*, 2003]. Inside the plasmasphere, hiss waves can cause losses everywhere, and plasmaspheric hiss appears to be driven by chorus waves reflecting into the plasmasphere from outside [*Bortnik et al.*, 2008].

In addition, PC-1 shows that the region from 200 keV to 2 MeV near $L_m \sim 3$ exhibits a large degree of variability. This reflects the motion of the inner edge of the outer zone, which is evident in Figure 20.

The second principal component, PC-2, is shown in Figure 23. The top panel is in the same format as Figure 22, and shows a node at $L_m \sim 4$, with antinodes at $L_m \sim 3$ and broadly over the outer zone. Because the node is a horizontal line at approximately constant L_m , PC-2 describes decoupling of the lower L shells from the higher ones. Specifically, this implies that radial diffusion is weaker than energy or pitch-angle diffusion, in a global context. The bottom panel illustrates that this feature is present across all pitch angles: the green isocontour is the node, and it is essentially a planar surface cutting

across energy and pitch angle dimensions at a nearly constant L_m . The second branch of the node, folding back to low L_m and progressively higher pitch angles represents the atmospheric loss cone, where the eigenvector is forced to zero as a boundary. PC-2 explains 18.2% of the variance.

Figure 24 shows PCs 3 and 4, which have somewhat hard-to-explain nodal structure. To some extent it is always tricky to interpret the higher-order PCs because they must be mathematically orthogonal to the lower order PCs even though the principal physical processes are correlated. In both PC 3 and 4 the node has more dependence on energy than in PC 2, suggesting some decoupling of higher and lower energies. PCs 3 and 4 appear to represent a combination of radial and energy decoupling, but the interpretation is somewhat ambiguous, as energy and L_m are not independent adiabatic invariants. In any case, there is no strongly pitch-angle dependent nodal structure in any of PC-1 through PC7, suggesting that, as expected, pitch angle diffusion is faster than both energy and radial diffusion. Based on the PCs, the ordering is: radial diffusion is slowest, pitch angle diffusion is fastest, and energy diffusion appears to be intermediate. This is consistent with published estimates [e.g., *Shprits et al.*, 2008a,b].

Along with the energy/spatial patterns, like those shown in Figures 22-24, each PC has a time series of amplitudes. Figures 25 and 26 show the time series of all eight PC amplitudes along with observed conditions for two of the so-called GEM storms (named for NSF's Geospace Environment Modeling program, which identified these storms for coordinated study). In the October 1998 storm, (Figure 25) PC-1 shows a gradual increase over several days associated with the main phase of the storm (October $\sim 19^{\text{th}}$), but preceding the peak solar wind speed (V_{sw}). PCs 2 and 3 make complementary excursions during the main phase, likely associated with the reconfiguration of the global magnetic field. Although the GOES >2 MeV electron flux shows a fairly straightforward 2-3 order of magnitude increase in flux superimposed on diurnal variations, the PCs reveal a far more complex global response. In most cases, the PCs do not return to near their prestorm values, suggesting global reconfiguration of the electron radiation belt topology.

In the October 2000 storm (Figure 26), again PC-1 shows a gradual increase over several days. PCs 2 and 3 also show the same characteristic complementary variations during the main phase (October $\sim 5^{\text{th}}$). As before, the PCs reveal a more complex response than the simple increase in intensity one would assume viewing the GOES data.

Statistical analysis of the PC amplitudes can reveal associations with other geophysical phenomena. Figure 27 shows the rank order prediction efficiency (the square of the rank order correlation coefficient) between the posterior PCs and three other phenomena. The GOES > 2 MeV electron flux is correlated with all of the first 5 PCs. The simplest interpretation of this result is that the environment at GEO responds to a variety of physical processes, and is coupled to dynamics at other locations. Nonetheless, the strong correlation of GOES with PC 2 is not surprising, given that PC 2 appears to represent decoupling of the inner and outer zones, and GOES resides far from the inner zone.

The magnetic storm-time disturbance index Dst can explain up to about 13% of the variance of PC-3, and about 5% of the variance of PCs 1, 2, and 6. The simplest interpretation of this result is that PCs 1, 2, 3, and 6 combine to describe the adiabatic response of the electron belts to global magnetic field reconfigurations.

Finally, Figure 27 shows that only PCs 1 and 3 have much association with the solar wind speed. However, this analysis accounts only for the immediate correlation. To obtain a more complete understanding of the relationships between the PCs and the solar wind speed, we must examine lagged correlations.

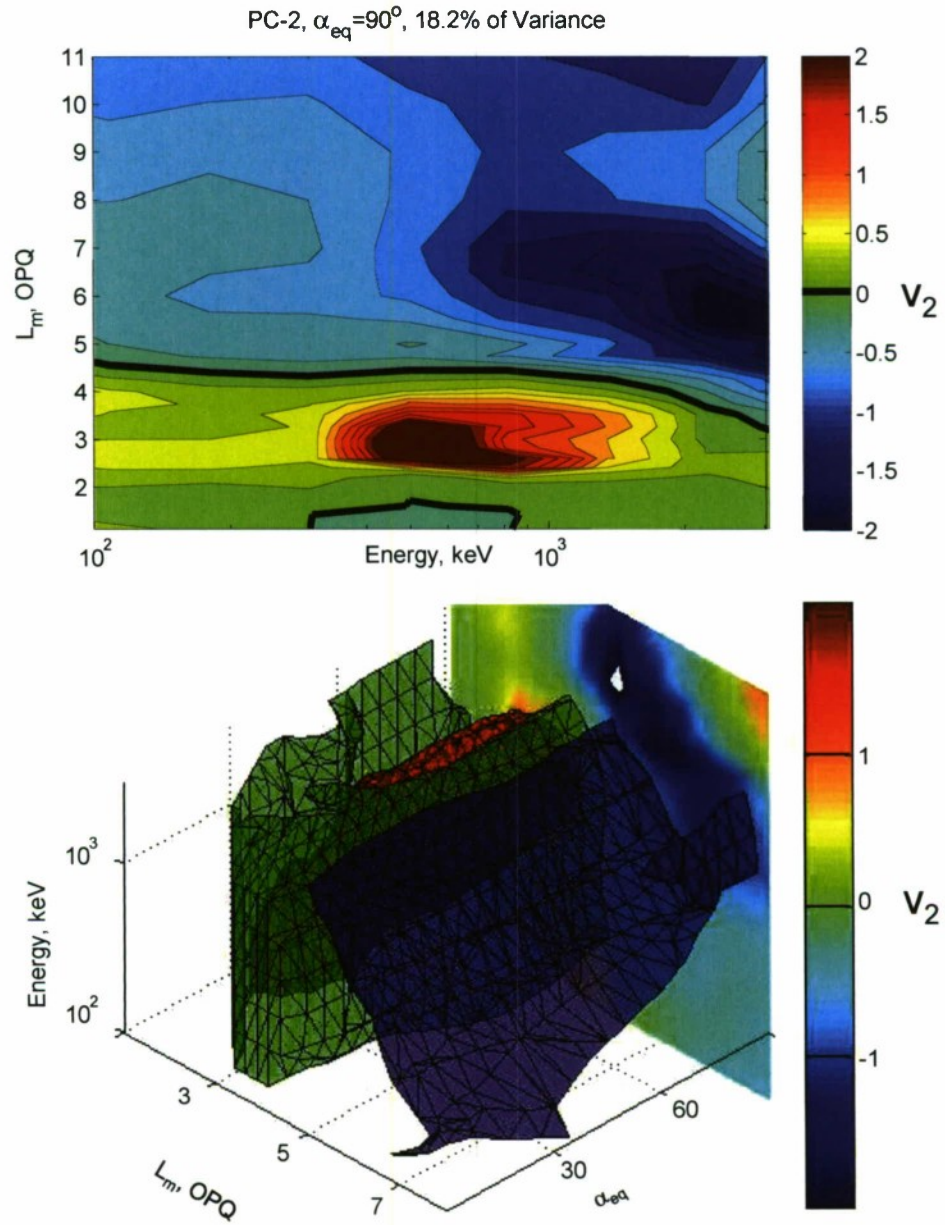


Figure 23: The second posterior principal component of the TEM-2 reanalysis. Top: equatorially mirroring electrons. Bottom: selected isocontours.

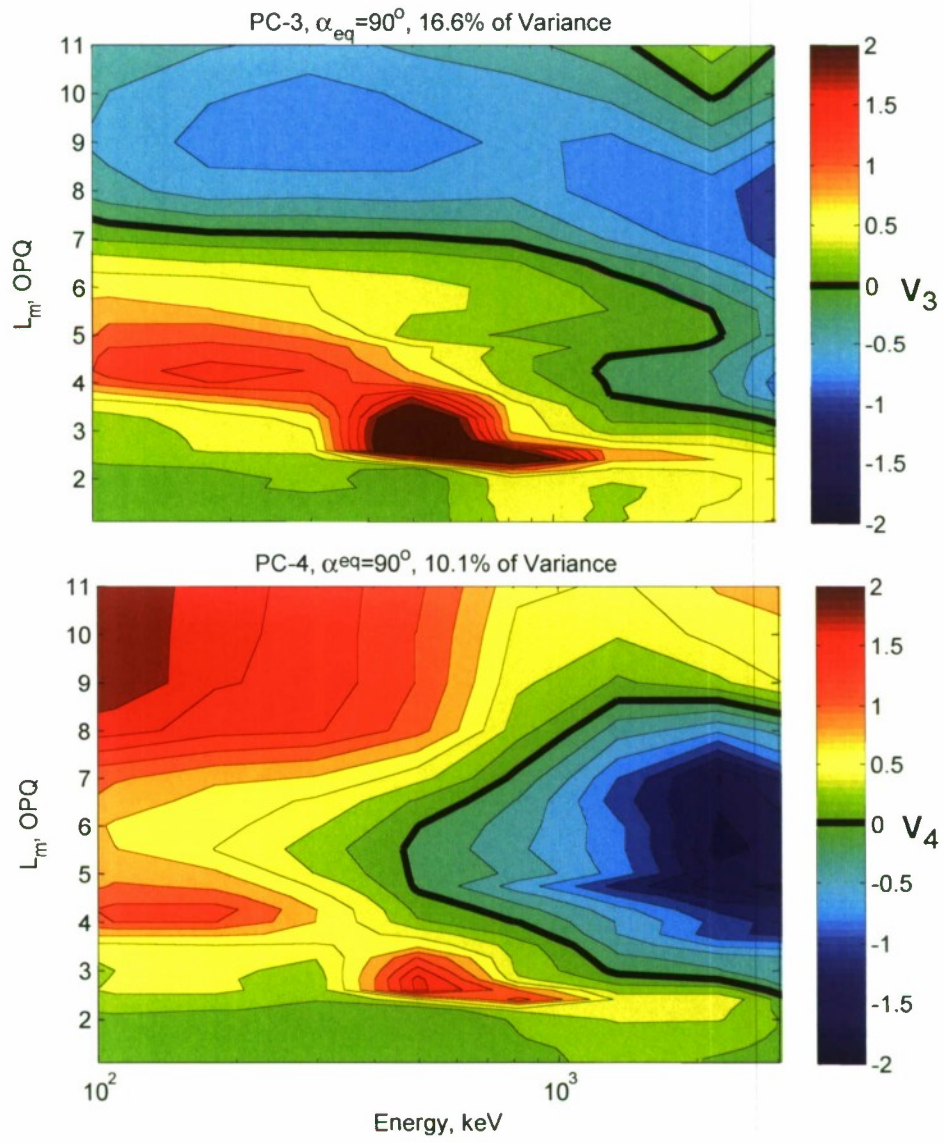


Figure 24: The third and fourth posterior principal components of the TEM-2 reanalysis, for equatorially mirroring electrons.

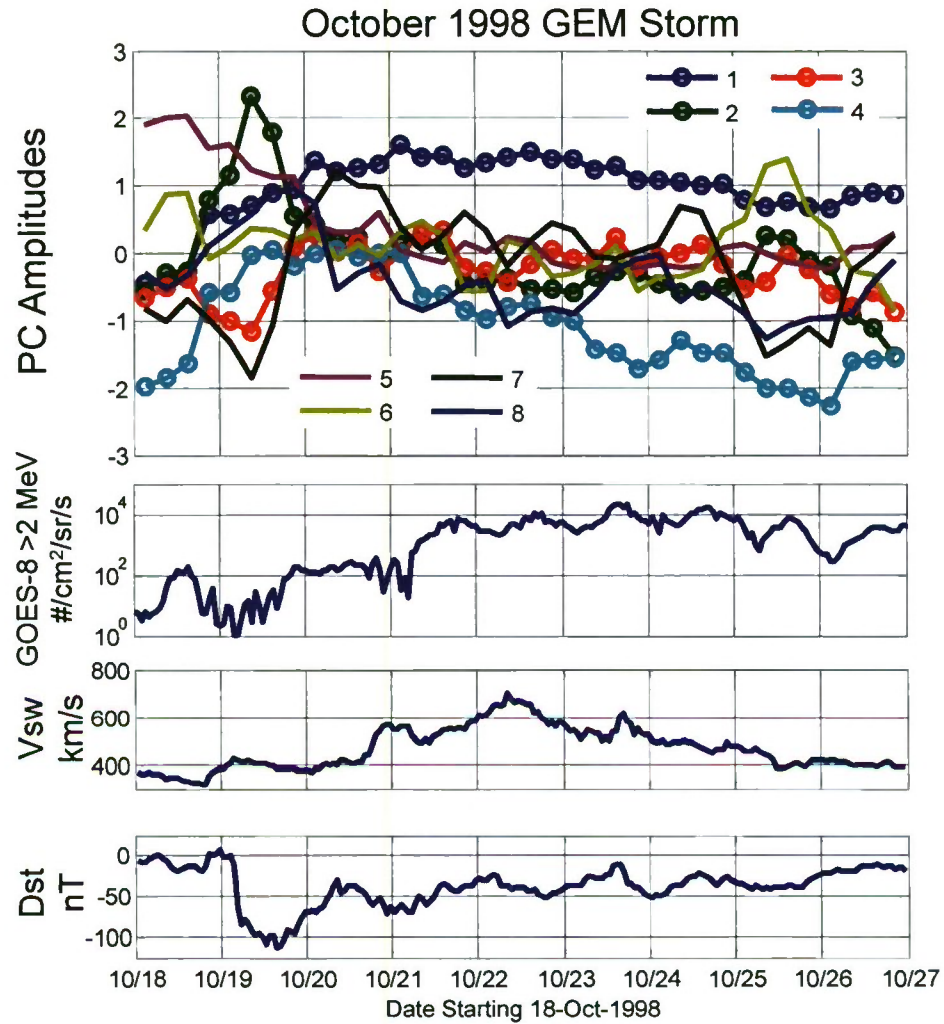


Figure 25: Top: TEM-2 reanalysis posterior principal components during the October 1998 GEM storm. Lower panels: observed electron flux at GEO, observed solar wind speed, and the magnetic storm-time disturbance index *Dst*.

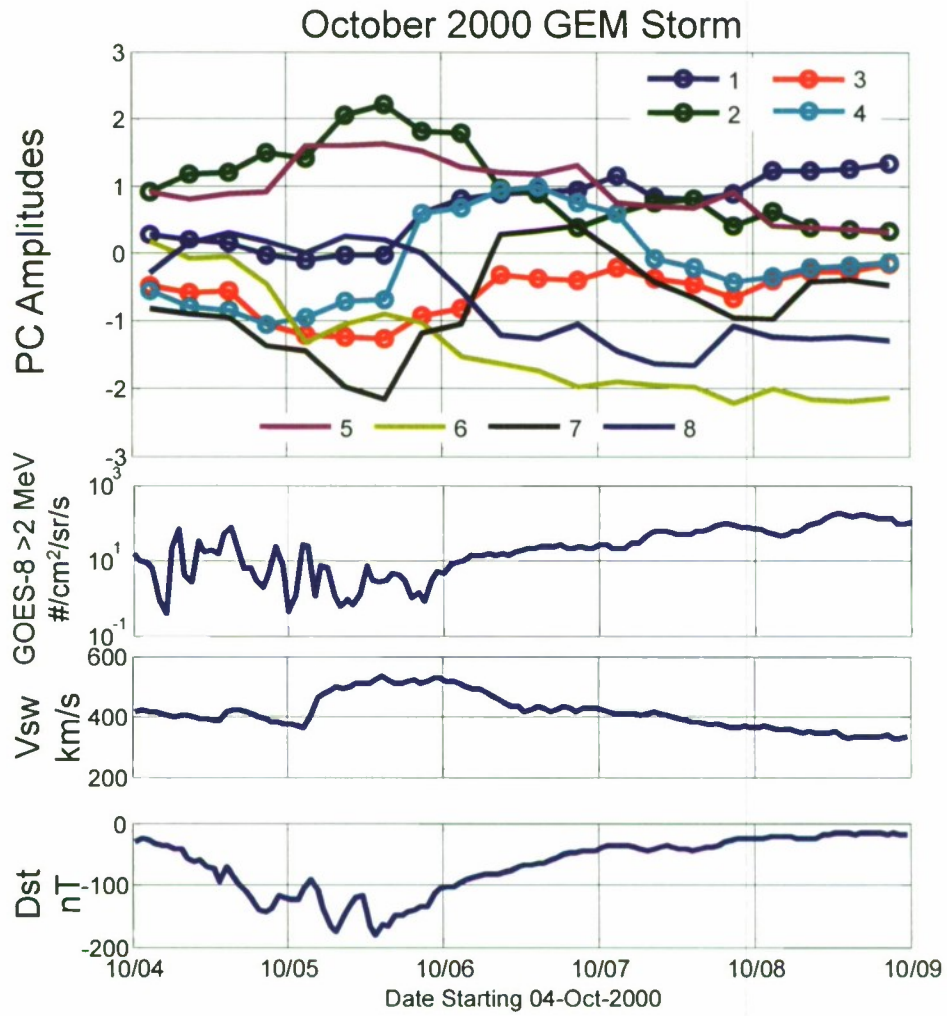


Figure 26: TEM-2 reanalysis posterior principal components and measurements during the October 2000 GEM storm, in the format of Figure 25.

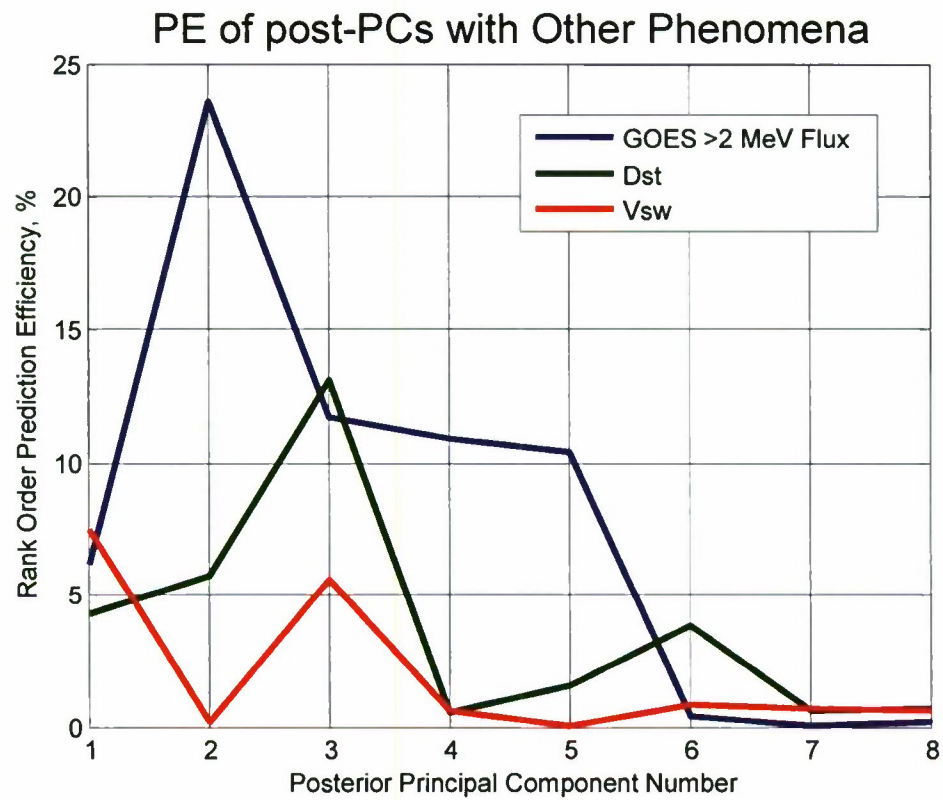


Figure 27: Prediction efficiency of TEM-2 reanalysis posterior principal components with respect to GOES > 2 MeV electron flux, *Dst*, and solar wind speed (*Vsw*).

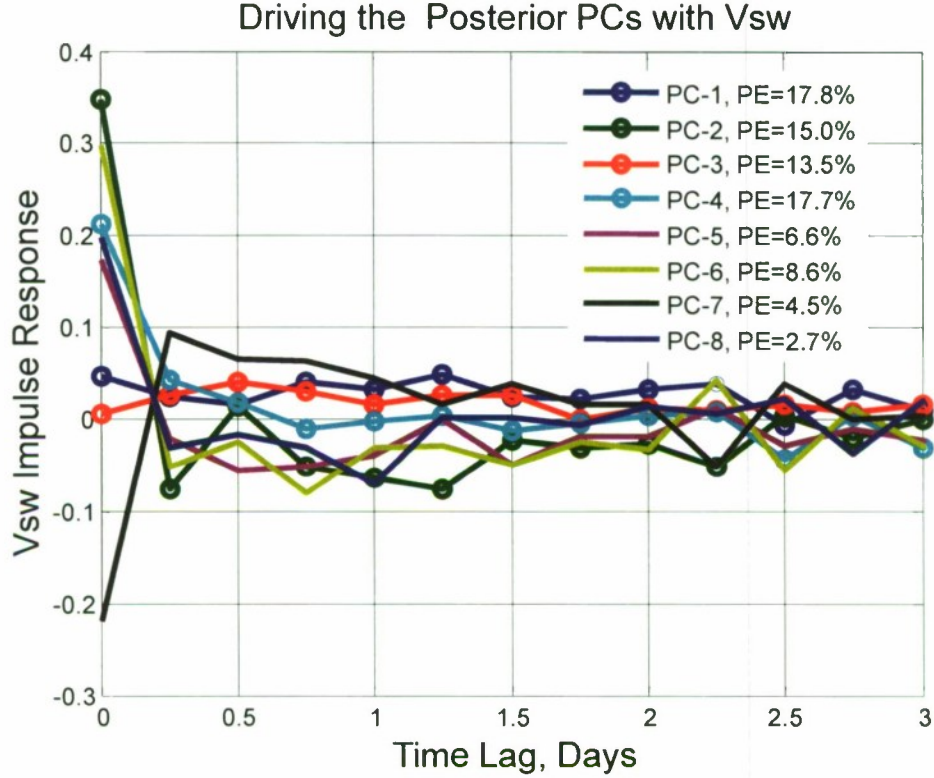


Figure 28: Impulse response of TEM-2 reanalysis posterior principal components with solar wind speed.

Assuming that each PC has an independent, possibly time-delayed response to the solar wind, we have computed the finite impulse response function for each PC to solar wind speed. Figure 28 shows how solar wind speed drives the PCs. With the exceptions of PCs 1 and 3, all the PCs have a strong initial response to V_{sw} . Of those, all but PC 4 have a bipolar response – quickly switching sign and remaining at the opposite sign for up to 2 days, ultimately leading to recovery. PCs 1 and 3 seem to have small, but persistently positive responses, consistent with a moving average process. PC 4, on the other hand, resembles a classic first-order autoregressive process, with a quasi-exponential impulse response. Accounting for time lag, the solar wind speed describes relatively more of the variance of the first 4 PCs than the last 4, with PCs 1 and 4 slightly edging out components 2 and 3.

One could extend the type of multivariate time series analysis shown in Figure 28 to develop a global radiation belt forecast model, as opposed to the GEO-specific models that are common today [e.g., *Ukhorskiy et al.*, 2004; *Rigler et al.*, 2004; *Li et al.*, 2001; *Baker et al.*, 1990]. Specifically, one can attempt to model or forecast the 8 PCs only, rather than attempting to model the thousands of points in the model grid. In essence, each PC becomes an index of radiation belt dynamics, which can be modeled in its own right, or alongside the other PCs. A similar approach is taken with the principal components of climate variability, such as the El Niño Southern Oscillation [see, e.g., *Latif et al.*, 1998].

Vassiliadis et al. [2002, 2003, 2005] have performed a related analysis on SAMPEX/PET data. In particular, they have identified principal regions of correlated response to magnetospheric and interplanetary parameters in one dimension (L_m). Their analysis could easily be applied to principal components or to the global reanalysis fluxes in 3 dimensions.

6 Summary

We have developed and demonstrated a global trapped electron radiation environment model: TEM-2. This model comes in two forms: a Monte Carlo scenario model and a Reanalysis. These two elements prototype the main components of future AE9/AP9 radiation specification models. Whereas the quantitative performance of the models is often less than one would desire for engineering or scientific work, the prototype demonstrates the analysis and run-time algorithms that carry the problem from an observed time series of unidirectional differential fluxes to an engineering user application. Further, the Reanalysis, or “standard solar cycle” provides a testbed for new scientific analysis algorithms, in particular principal component analysis.

We expect some improvements upon the algorithms shown here before the release of the AE9/AP9 beta and subsequent versions:

- The AE9/AP9 beta models use a drift-invariant K, Φ coordinate system in place of the α_{eq}, L_m system of TEM-2. The AE9/AP9 beta will still use the OPQ model.
- The AE9/AP9 beta will implement a revision to equation (20) which will account for the observation errors explicitly (as opposed to implicitly in the weighted sum).
- The AE9 beta will use more data sets than were used in TEM-2, in particular it will add LANL GEO and GPS data.
- Due to the finer grid resolution in AE9 and AP9, the calculation of the principal components will be performed on a reduced grid and the energy/spatial patterns interpolated onto a finer grid. This extra step reduces the computational resources needed to construct and factor the spatial covariance matrix $\underline{\underline{\Sigma}}$.
- The nearest neighbors interpolation algorithm will be modified to provide an inherently smoother $\vec{\theta}$.
- The bootstrapping used to determine $\underline{\underline{S}}$ will be expanded to including randomization over interpolation and extrapolation algorithms and assumptions (e.g., spectral shapes).

The AE9/AP9 beta, like TEM-2 will still not have fully-validated, intercalibrated data. That, along with more data sets and the introduction of a low-altitude grid, will have to wait for AE9/AP9 version 1.0.

A TEM-1

TEM-1 [described briefly in *O'Brien, 2008*] was built from S3-3 MES and CRRES MEA/HEEF data only. The statistical tables and scenario generation algorithms were essentially the same as those in TEM-2. However, the data processing (i.e., Figure 3) was considerably different.

The nearest neighbors interpolation algorithms were not used. Instead the flux maps were built by fitting a neural network to the observations. Also, $\tilde{\theta}$ was defined simply as $(\log m_{50}, \log m_{95})$, which proved to be a mistake – it did not explicitly disallow $m_{95} > m_{50}$, especially in the perturbed maps. In addition, the perturbations to $\tilde{\theta}$ were problematic with the neural network because the error covariance matrix for the network’s free parameters was often singular, leading us to have to use less accurate networks with non-singular error covariance (we have since learned how to circumvent this singularity by factoring the error covariance matrix into its leading principal components).

The spatial covariance was obtained by fitting a simple analytical function, with an independent exponential decay in $\log E$, α_{eq} , and L_m . We could not successfully build neural networks for the covariance because it we could not find an economical way to constrain either unity along the diagonal or positive definite-ness.

In TEM-1 we made some attempts to intercalibrate the data sets statistically, but those were abandoned because they were too ad hoc, and because S3-3 MES and CRRES/MEA were already likely adequately intercalibrated by Vampola on the ground before launch. From TEM-2 onward, data intercalibration processes are considered separate from the model construction.

A final lesson that TEM-1 taught us was that run-time speed depends strongly on the speed of computing the magnetic coordinates. In particular computing L_m requires tracing a magnetic field line, and, looking to the AE9/AP9 models, computing Φ would require many field line traces. We adopted fast algorithms attributed to K. Pfizter for computing the integral invariant I behind L_m [*McIlwain, 1961*]. This also began a line of research toward fast Φ algorithms using analytical functions and eventually neural networks [similar to *Koller et al., 2009*].

With the TEM-1 lessons learned in mind, TEM-2 was developed from scratch as a generic “Next Generation Radiation Specification”, with algorithms that could accommodate changes in the grid coordinates, particle species, etc. TEM-1 proved invaluable in identifying where the tough problems were both from an algorithmic and a computational perspective.

B Useful derivatives

In the numerical optimization, we need expressions for the first and second derivatives of our probability equations. We start with a restatement of the negative log likelihood function from (48) with generic marginal distribution:

$$\begin{aligned}\ell &= \sum_k \hat{\ell}(\lambda_k) - \sum_i [\log x_i + \log f_i(x_i)] \\ &\quad + \frac{1}{2}(\vec{q}^T \vec{q} - \vec{z}^T \vec{z}) + \text{constants.}\end{aligned}\tag{92}$$

The optimization relies on derivatives of ℓ with \vec{q} :

$$\begin{aligned}\frac{\partial \ell}{\partial q_j} &= \sum_k \frac{\partial \hat{\ell}_k}{\partial \lambda_k} \frac{\partial \lambda_k}{\partial q_j} + q_j, \\ &\quad - \sum_i z_i Q_{ij} + \left[\frac{f'_i(x_i)}{f_i(x_i)} + \frac{1}{x_i} \right] \frac{\partial x_i}{\partial q_j},\end{aligned}\tag{93}$$

$$\frac{\partial \lambda_k}{\partial q_j} = \sum_i \frac{\partial \lambda_k}{\partial x_i} \frac{\partial x_i}{\partial q_j} = \sum_i H_{ki} \frac{\partial x_i}{\partial q_j},\tag{94}$$

$$\frac{\partial x_i}{\partial q_j} = \frac{\partial x_i}{\partial z_i} \frac{\partial z_i}{\partial q_j} = \frac{\partial x_i}{\partial z_i} Q_{ij} = \frac{\phi(z_i)}{f_i(x_i)} Q_{ij}.\tag{95}$$

In the special case of Weibull x , we have:

$$\begin{aligned}\ell &= \sum_k \hat{\ell}_k(\lambda_k) + \frac{1}{2}(\vec{q}^T \vec{q} - \vec{z}^T \vec{z}) \\ &\quad - \sum_i \gamma_i \log x_i - (x_i/x_{0,i})^{\gamma_i} + \text{constants},\end{aligned}\tag{96}$$

$$\begin{aligned}\frac{\partial \ell}{\partial q_j} &= \sum_k \frac{\partial \hat{\ell}_k}{\partial \lambda_k} \frac{\partial \lambda_k}{\partial q_j} + q_j \\ &\quad - \sum_i z_i Q_{ij} + \left[\gamma_i/x_i - \gamma_i x_i^{\gamma_i-1}/x_{0,i}^{\gamma_i} \right] \frac{\partial x_i}{\partial q_j}.\end{aligned}\tag{97}$$

In the special case of log-normal x , we have:

$$\ell = \sum_k \hat{\ell}_k(\lambda_k) + \frac{1}{2}\vec{q}^T \vec{q} + \text{constants},\tag{98}$$

$$\frac{\partial \ell}{\partial q_j} = \sum_k \frac{\partial \hat{\ell}_k}{\partial \lambda_k} \frac{\partial \lambda_k}{\partial q_j} + q_j,\tag{99}$$

$$\frac{\partial x_i}{\partial q_j} = (x_i \sigma_i) Q_{ij}.\tag{100}$$

References

- , Avoiding problems caused by spacecraft on-orbit internal charging effects, NASA-HDBK-4002, NASA 1999.
- , International Geomagnetic Reference Field. <http://www.ngdc.noaa.gov/IAGA/vmod/igrf.html>, IAGA and NGDC, 2009.
- Baker, D. N., R. L. McPherron, T. E. Cayton, and R. W. Klebesadel, Linear prediction filter analysis of relativistic electron properties at 6.6 R_E , *J. Geophys. Res.*, *95*(15), 133-15,140, 1990.
- Blake, J.B., et al., CEPPAD, *Spacc Sci. Rev.*, *71*, 531-562, 1995.
- Bortnik, J., R.M. Thorne, and N.P. Meredith, (2008) The unexpected origin of plasmaspheric hiss from discrete chorus emissions, *Nature*, *452*, 62-66, doi:10.1038/nature06741.
- Bourdarie, S., A. Sicard-Piet, R. Friedel, T. P. O'Brien, T. Cayton, B. Blake, D. Boscher, and D. Lazaro, Outer Electron Belt Specification Model, *IEEE Trans. Nucl. Sci.*, *56*(4), 2009, 2251-57.
- S. Bourdarie, D. Lazaro, A. Hands, K. Ryden, P. Nieminen, (2010) Electron environment specification models for navigation orbits, proceedings of RADECS 2009, in press.
- Brautigam, D. H., and J. T. Bell, CRRESELE Documentation, PL-TR-95-2128, *Environmental Research Papers*, 1178, Phillips Laboratory, 1995.
- Cook, W.R., et al., PET: A proton/electron telescope for studies of magnetospheric, Solar, and galactic particles, *IEEE Trans. Geosci. and Remote Sens.*, *31*(1), 565-571, 1993.
- Daly, E. J., et al., Problems with models of the radiation belts, *IEEE Trans. Nucl. Sci.*, *43*, 403-415, 1996.
- DeMajistre, R., E. C. Roelof, P. Cison Brandt, and D. G. Mitchell (2004), Retrieval of global magnetospheric ion distributions from high-energy neutral atom measurements made by the IMAGE/HENA instrument, *J. Geophys. Res.*, *109*, A04214, doi:10.1029/2003JA010322.
- Dichter, B.K., F.A. Hanser, B. Sellers, and J.L. Humerwadel, High Energy Electron Fluxmeter, *IEEE Trans. Nucl. Sci.*, *40*(2), 252- 255, 1993.
- Fennell, J.F., et al., Internal Charging: A preliminary environmental specification for satellites, *IEEE Trans. Plasma Sci.*, *28*(6) 2029, 2000.
- Gussenhoven, M.S. et al., Near-earth radiation belt deficiencies as seen on CRRES, *Adv. Spacc Res.*, *14*(10) 927-941, 1994.
- Kauekal, S. G., D. N. Baker, and J. B. Blake, Multisatellite measurements of relativistic electrons: Global coherence, *J. Geophys. Res.*, *106*, 29,721-29,732, 2001.
- Kim, H.-J., and A. A. Chan, Fully adiabatic changes in storm time relativistic electron fluxes, *J. Geophys. Res.*, *102*, 22,107-22,116, 1997.
- Koller, J., Y. Chen, G. D. Reeves, R. H. W. Friedel, T. E. Cayton, and J. A. Vrngrt (2007), Identifying the radiation belt source region by data assimilation, *J. Geophys. Res.*, *112*, A06244, doi:10.1029/2006JA012196.
- Koller, J., Reeves, G. D., and Friedel, R. H. W.: LANL* V1.0: a radiation belt drift shell model suitable for real-time and reanalysis applications, *Geosci. Model Dev. Discuss.*, *2*, 159-184, 2009.

- Latif, M., D. Anderson, T. Barnett, M. Cane, R. Kleeman, A. Leetmaa, J. O'Brien, A. Rosati, and E. Schneider (1998), A review of the predictability and prediction of ENSO, *J. Geophys. Res.*, 103(C7), 14375-14393.
- Li, X, M. Temerin, D.N. Baker, G.D. Reeves, and D. Larson, Quantitative prediction of radiation belt electrons at geostationary orbit based on solar wind measurements *Geophys. Res. Lett.* 28(9), 1887-1890, doi:10.1029/2000GL012681, 2001.
- Maget, V., S. Bourdarie, D. Boscher, and R. H. W. Friedel (2007), Data assimilation of LANL satellite data into the Salammbô electron code over a complete solar cycle by direct insertion, *Space Weather*, 5, S10003, doi:10.1029/2007SW000322.
- McIlwain, C.E., Coordinates for mapping the distribution of magnetically trapped particles, *J. Geophys. Res.*, 66(11), 3681-91, 1961.
- Millan, R.M., R.M. Thorne, Review of radiation belt relativistic electron losses, *J. Atmos. Sol. Terr. Phys.*, 69, 362-377, doi:10.1016/j.jastp.2006.06.019.
- Moldwin, M. B., S. Mayerberger, H. K. Rassoul, T. Barnicki, and R. R. Anderson, Plasmopause response to geomagnetic storms: CRRES results, *J. Geophys. Res.*, 108(A11), 1399, doi:10.1029/2003JA010187, 2003.
- Nelson, R.B., *An Introduction to Copulas (Lecture Notes in Statistics, 139)*, Springer, New York, 1999.
- Ni, B., Y. Shprits, T. Nagai, R. Thorne, Y. Chen, D. Kondrashov, and H.-J. Kim (2009), Reanalyses of the radiation belt electron phase space density using nearly equatorial CRRES and polar-orbiting Akebono satellite observations, *J. Geophys. Res.*, 114, A05208, doi:10.1029/2008JA013933.
- O'Brien, T. P., A framework for next-generation radiation belt models, *Space Weather*, 3, S07B02, doi:10.1029/2005SW000151, 2005.
- O'Brien, T.P., Trapped Electron Model 1 (TEM-1) status report – alpha version. ATR-2008(5236)-1, The Aerospace Corporation, El Segundo, CA, 2008.
- O'Brien, T. P., J. F. Fennell, J. L. Roeder, and G. D. Reeves (2007), Extreme electron fluxes in the outer zone, *Space Weather*, 5, S01001, doi:10.1029/2006SW000240.
- Olson, W. P., and K. A. Pfitzer, A quantitative model of the magnetospheric magnetic field, *J. Geophys. Res.*, 79, 3739, 1974.
- Perez, J. D., X.-X. Zhang, P. C:son Brandt, D. G. Mitchell, J.-M. Jahn, and C. J. Pollock (2004), Dynamics of ring current ions as obtained from IMAGE HENA and MENA ENA images, *J. Geophys. Res.*, 109, A05208, doi:10.1029/2003JA010164.
- Reagan, J.B. R.W. Nightingale, E.E. Gaines, and W.L. Imhof, Outer zone energetic electron spectral measurements, *J. Spacecraft*, 18(1), 83-88, 1981.
- Rigler, E. J., D. N. Baker, R. S. Weigel, D. Vassiliadis, and A. J. Klimas (2004), Adaptive linear prediction of radiation belt electrons using the Kalman filter, *Space Weather*, 2, S03003, doi:10.1029/2003SW000036.
- Schulz, M. and L.J. Lanzerotti, *Particle Diffusion in the Radiation Belts*, Springer-Verlag, New York, 1974.
- Shprits, Y., D. Kondrashov, Y. Chen, R. Thorne, M. Ghil, R. Friedel, and G. Reeves (2007), Reanalysis of relativistic radiation belt electron fluxes using CRRES satellite data, a radial diffusion model, and a Kalman filter, *J. Geophys. Res.*, 112, A12216, doi:10.1029/2007JA012579.

- Shprits, Y. Y., S. R. Elkington, N. P. Meredith, and D. A. Subbotin, (2008a), Review of modeling of losses and sources of relativistic electrons in the outer radiation belts I: Radial transport, *J. Atmos. Sol. Terr. Phys.*, *70*, 1694-1713, doi:10.1016/j.jastp.2008.06.014.
- Shprits, Y. Y., D. A. Subbotin, N. P. Meredith, and S. R. Elkington (2008b), Review of modeling of losses and sources of relativistic electrons in the outer radiation belts II: Local acceleration and loss, *J. Atmos. Sol. Terr. Phys.*, *70*, 1694-1713, doi:10.1016/j.jastp.2008.06.014.
- Sicard-Piet, A., S. Bourdarie, D. Boscher, R. H. W. Friedel, M. Thomsen, T. Goka, H. Matsumoto, and H. Koshiishi (2008), A new international geostationary electron model: IGE-2006, from 1 keV to 5.2 MeV, *Space Weather*, *6*, S07003, doi:10.1029/2007SW000368.
- Sicard-Piet A., S. Bourdarie, D. Boscher, R. Friedel, T. Cayton, Solar Cycle Electron Radiation Environment at GNSS Like Altitude, Proceedings 57th International Astronautical Congress, Valencia, Sept 2006. Available in IRBEM-LIB, <http://irbem.sourceforge.net/>.
- Tribble, A.C., et al., The space environment and survivability, in *Space Mission Analysis and Design*, 3rd ed., J.R. Wertz and W.J. Larson eds., Kluwer, Boston, 203-221, 1999.
- Ukhorskiy, A. Y., M. I. Sitnov, A. S. Sharma, B. J. Anderson, S. Ohtani, and A. T. Y. Lui (2004), Data-derived forecasting model for relativistic electron intensity at geosynchronous orbit, *Geophys. Res. Lett.*, *31*, L09806, doi:10.1029/2004GL019616.
- Vampola, A. L., *Outer Zone Energetic Electron Environment Update*, Final Report of ESA/ESTEC Contract No. 151351, 1996.
- Vampola, A.L., and C.D. Adams, Outer zone electron precipitation produced by a VLF transmitter, *J. Geophys. Res.*, *93*(A3), 1849-1858, 1998.
- Vampola, A.L., J.V. Osborn, and B.M. Johnson, CRRES Magnetic Electron Spectrometer AFGL-701-5A (MEA), *J. Spacecr. Rockets*, *29*(4), 592-595, 1992.
- Vassiliadis, D., A. J. Klimas, S. G. Kanekal, D. N. Baker, and R. S. Weigel, Long-term-average, solar cycle, and seasonal response of magnetospheric energetic electrons to the solar wind speed, *J. Geophys. Res.*, *107*(A11), 1383, doi:10.1029/ 2001JA000506, 2002.
- Vassiliadis, D., A. J. Klimas, R. S. Weigel, D. N. Baker, E. J. Rigler, S. G. Kanekal, T. Nagai, S. F. Fung, R. W. H. Friedel, and T. E. Cayton, Structure of Earth's outer radiation belt inferred from long-term electron flux dynamics, *Geophys. Res. Lett.*, *30*(19), 2015, doi:10.1029/ 2003GL017328, 2003.
- Vassiliadis, D., S. F. Fung, and A. J. Klimas (2005), Solar, interplanetary, and magnetospheric parameters for the radiation belt energetic electron flux, *J. Geophys. Res.*, *110*, A04201, doi:10.1029/2004JA010443.
- Vette, J.I., K.W. Chan, and M.J. Teague, Problems in Modeling the Earth's Trapped Radiation Environment, AFGL-TR-78-0130, Hanscom AFB, MA, 1978. 91-29, 1978.
- Vette, J. I., The AE-8 Trapped Electron Model Environment, NSSDC/WDC-A-R&S 91-24, 1991.
- Wilks, D. S., *Statistical Methods in the Atmospheric Sciences: An Introduction*, Academic Press, New York, 1995.
- Zwiers, F.W., and H. von Storch, Taking serial correlation into account in tests of the mean, *J. Climate*, *9*, 336, 1995.